NUMERICAL MODELLING OF FAILURE IN 3D QUASI-BRITTLE UNREINFORCED STRUCTURAL COMPONENTS

A Thesis Submitted to
the Graduate School of Engineering and Sciences of
İzmir Institute of Technology
in Partial Fulfillment of the Requirements for the Degree of

MASTER OF SCIENCE

in Civil Engineering

by
Bekir KAÇMAZ

July 2022
İZMİR

ACKNOWLEDGMENTS

I would like to thank to my advisor Assoc. Prof. Dr. İzzet Özdemir for his endless support, patients and valuable effort. Without his experience and guidance, it may not be possible to complete this thesis. I will be honored to have worked with him during my life.

I would also have to thank to my dear colleagues Süleyman Yaşayanlar and Yonca Yaşayanlar for all their support during this journey.

Furthermore, I am thankful to my beloved wife and my family for their precious support and encouragement.

Finally, this study is supported by the Scientific and Technological Research Council of Turkey (TÜBİTAK) under grant number 121M121. I would like to acknowledge this support.

ABSTRACT

NUMERICAL MODELLING OF FAILURE IN 3D QUASI-BRITTLE UNREINFORCED STRUCTURAL COMPONENTS

Concrete has been one of the most commonly used modern structural material with quasi-brittle response. Because of its wide usage, numerical prediction of crack path and failure of structural components made of concrete and reinforced concrete has a great importance. To achieve this goal, a wide range of techniques have been introduced by treating fracture differently. In addition, the development of successful element formulations in analysis of 3D structural components has also been an active research topic. Several formulations have been proposed as an alternative to the conventional Lagrangian elements in recent years.

In this thesis, localizing implicit gradient damage model and an isogemetric tetrahedral element are combined to investigate failure of 3D quasi-brittle unreinforced structural components. 10 noded Bézier tetrahedral element is implemented to commercial finite element software Abaqus through user defined element subroutine, UEL. The implementation is validated by using two benchmark problems with nearly incompressible linear elastic and elasto-plastic material behaviors. After validating the implemented element, the formulation is extended such that localizing implicit gradient damage model is embedded within the isogeometric element formulation. Resulting two field formulation is tested on 3D experimental studies that exhibit complex fracture propagation due to combined torsional and bending moments. The sufficiency of the implemented two field formulation is verified by comparing obtained results with the experimental ones in terms of both force versus displacement responses and resulting crack paths.

ÖZET

3 BOYUTLU YARI GEVREK DONATISIZ YAPISAL ELEMANLARDA GÖÇMENİN SAYISAL MODELLENMESİ

Beton tüm Dünya'da en yaygın olarak kullanılan ve yarı gevrek davranış gösteren yapı malzemelerinden biridir. Bu yoğun kullanım nedeniyle beton ve betonarme yapısal elemanların sayısal göçme analizlerinin başarılı şekilde yapılması büyük önem arz etmektedir. Bu amaçla, çatlakları farklı yöntemler kullanarak temsil eden birçok teknik ortaya konulmuştur. Ayrıca üç boyutlu yapısal elemanların analizi için başarılı eleman formülasyonlarının geliştirilmesi de oldukça önemlidir. Bu nedenle son yıllarda birçok formülasyon geleneksel Lagrange elemanlarına alternatif olarak öne sürülmüştür.

Bu tezde, lokalize olan örtük gradyant hasar yaklaşımı ve izogeometrik eleman formülasyon birleşiminin üç boyutlu yarı gevrek donatısız yapısal elemanların modellenmesinde ne derece başarılı olabileceği ele alınmıştır. Bahsedilen 10 düğüm noktalı Bézier dört yüzlü eleman formülasyonu Abaqus sonlu elemanlar yazılımı içerisine UEL altyordamı (User ELement subroutine : kullanıcı tarafından tanımlanan eleman altyordamı) yardımıyla entegre edilmiştir. Bu entegrasyon sıkıştırılamazlık limitine çok yakın doğrusal elastik ve elasto-plastik davranışa sahip iki adet problem ile sınanmıştır. Kontrol sonrası entegrasyonu yapılan elemana lokalize olan gradyant tipi örtük hasar modeli eklenmiştir. Ortaya çıkarılan iki alanlı bu eleman formülasyonu ile birleşik eğilme ve burulma etkisi altında karmaşık çatlak oluşumları içeren üç boyutlu deneysel çalışmalar analiz edilmiştir. Nümerik sonuçlar ile elemanın performansı hem kuvvet-yer değiştirme hem de çatlak gelişimleri açısından deneysel çalışma sonuçları ile karşılaştırılmıştır.

TABLE OF CONTENTS

LIST OF FIGURES

Figure **Page**

Figure **Page**

Figure **Page**

LIST OF TABLES

LIST OF ABBREVIATIONS

CAD . . . . . Computer Aided Design
CIGD . . . . . Conventional Implicit Gradient Damage
CMOD . . . . . Crack Mouth Opening Displacement
FEA . . . . . Finite Element Analysis
FEM . . . . . Finite Element Method
IGA . . . . . Isogeometric Analysis
LIGD . . . . . Localizing Implicit Gradient Damage
NURBS . . . . . Non-Uniform Rational B-Splines
SDV . . . . . Solution Dependent Variables

CHAPTER 1

INTRODUCTION

Predicting the failure of structural components has been a central theme in structural analysis and design. While fracture is brittle for some materials such as glass, the failure of metals is ductile. However, failure process of quasi-brittle materials consists of a softening region which is followed by the complete failure of the material. Concrete is one of the most commonly used structural material on earth with quasi-brittle response. Therefore, predicting the formation of crack and failure for concrete and reinforced concrete structural components is important. The methods used for modelling the failure of quasi-brittle materials can be roughly divided into three parts. Depending on the kinematics used to define crack, these methods can be classified as continuous, discontinuous and combined. In continuous methods, fracture is not taken as a discontinuity and considered by using a damage variable which allows the formation of softening bands within the body. On the contrary, in discontinuous methods, fracture is defined as a discontinuity in kinematic description by means of additional degrees of freedom. Extended finite element (X-FEM) method is one of most widely used of discontinuous methods (Khoei, 2015). Finally, in the combined methods the softening branch is considered with the help of continuous approach, until the crack initiation. Thereafter, fracture is inserted to the problem as a discontinuity by using X-FEM (Mediavilla Varas, 2005). Because of their relatively easier implementation in the existing finite element solution algorithms, continuous approaches have been widely used. However, it was figured out that the solutions obtained by using classical continuum damage models do not converge to physically meaningful results in early 80s (Bažant et al., 1984). One of the proposed solutions to overcome this problem was to use non-local formulations. The approach that stands out among these non-local proposals is implicit gradient damage formulation. Even though the pathological mesh dependency problem could be prevented with the usage of this approach, it has been observed that the resulting damage distributions tend to widen artificially. In order to eliminate this problem, thermodynamically consistent localizing implicit gradient damage (LIGD) model was proposed (Poh and Sun, 2017).

However, the accuracy of this model on non-planar fractures of 3D quasi-brittle structural components has not been fully investigated yet.

On the other hand, efficient element formulations are needed for solutions of 3D problems. In this context, besides traditional isoparametric Lagrangian element formulations, there are also element formulations based on the recently proposed isogeometric analysis (IGA). IGA is a revolutionary approach that was introduced by Hughes in the 2000s and aims to change completely traditional methods (Cottrell et al., 2009). In traditional approach, it is required to prepare CAD model of the analyzed part, import it to finite element solver, repair and create an appropriate mesh for analysis. IGA, on the other hand, is an approach based on the idea of using basis functions that are used to create the model in CAD model (B-Splines, NURBS) also in finite element analysis instead of Lagrange polynomials. In this approach, geometry approximation errors are almost completely eliminated. Due to higher continuity of B-Splines and NURBS, IGA has been successfully used in analysis of thin plates and shells. Efficient IGA elements for 3D solid bodies have been under development as well (Espath et al., 2011; Engvall and Evans, 2016). Especially, the formulation recently proposed by Kadapa seems to be an attractive approach, since it creates the control points from the nodes of 10 noded Lagrangian tetrahedral elements (Kadapa, 2019a). This also implies that, using the existing mesh generators with this isogeometric element formulation is possible. In this method, the aim is using Bernstein polynomials as basis functions which have higher continuity, rather than reducing the geometry approximation error. The performance of this element has been studied for nearly incompressible elasticity and elasto-plasticity. However, it is not yet known how successful this element is in failure and resulting crack path prediction of quasi-brittle structural components.

With this motivation, in this theses, selected 3D fracture problems are analyzed by using 10 noded Bézier tetrahedral element and localizing implicit gradient damage model. For this purpose, 10 noded Bézier tetrahedral element is implemented to commercial finite element analysis software Abaqus through user defined element (UEL) subroutine. Afterwards, LIGD model is embedded in this element and the resulting two field formulation is used to analyze 3D case studies involving planar and non-planar cracks.

1.1. Outline of the Thesis

In Chapter 2, the basis of continuum damage mechanics are laid out, path dependency problem is revisited and the solution of this issue is presented. Implicit gradient damage and localizing implicit gradient damage models are detailed and the resulting coupled equations are introduced both in strong and weak forms in this chapter as well. In Chapter 3, the basics of IGA are summarized and the implemented 10 noded Bézier element is introduced. Abaqus implementation of the element is also discussed and the implementation is tested by using two benchmark problems. In Chapter 4, four experiments are numerically analyzed with the mentioned formulation and the obtained results are compared with the experimental ones. In the last chapter, the thesis is concluded by the main findings and recommendations for future studies.

CHAPTER 2

CONTINUUM DAMAGE MECHANICS

As mentioned in Chapter 1, the main focus of this thesis is to construct a damage based failure model, which is suitable for quasi-brittle material response. The scope of the thesis is limited only to static cases and dynamic effects are not covered. The equilibrium equations in small strain context can be written as

$$\nabla \cdot \boldsymbol{\sigma} + \rho\, \boldsymbol{b} = \mathbf{0} \tag{2.1}$$

where $\boldsymbol{\sigma}$ is the stress tensor, $\boldsymbol{b}$ is the body force, ρ is the density and $\nabla\cdot$ is the divergence operator. To complete the problem and map it into a well-posed state, it is necessary to specify the boundary conditions. The surface of the solid body can be decomposed into two non-overlapping parts such as Γ_t and Γ_u over which tractions and displacements are prescribed, respectively. A constitutive model is necessary to specify the stress tensor. As far as modelling of failure in quasi-brittle materials is concerned, existing numerical models can be classified as discontinuous, continuous and combined.

Continuum damage mechanics is one of these models. In this approach, fracture does not contribute to the displacement field as a discontinuity. The stiffness of material decreases gradually depending on the damage variable which stands between zero and one. When the damage variable at a material point reaches to one, it is considered to be complete fracture. One of the most well known of the discontinuous models is the extended finite element (X-FEM) method (Khoei, 2015). In this method, fracture is embedded within kinematic description of the problem as a discontinuity. However in this method, it is required to add and remove some degrees of freedom dynamically according to the crack propagation path. In the combined methods, the softening is dealt with continuum damage mechanics. When the damage reaches to one at a material point, discontinuity is inserted in kinematics using X-FEM (Mediavilla Varas, 2005). In this thesis, continuum damage mechanics will be used because of its easier implementation

and robustness.

2.1. Continuum Damage Mechanics

The most widely used way to describe damage variable is the geometrical one. In an element with infinitesimal volume dV, which is large enough for containing a number of cracks, voids and defects, one surface can be named as dS. The defected and undefected areas on this surface are shown by dS^D and $dS^U = dS - dS^D$ respectively. The definition of the damage variable D with respect to these quantities is denoted as a ratio of the defected area over total area as

$$D = \frac{dS^D}{dS} \tag{2.2}$$

When the infinitesimal element dV is under a constant nominal stress state σ, the damaged area on surface dS of the element can not carry any load and nominal stress has to be carried only by the undamaged are $dS^U = dS - dS^D$. It is obvious that the effective stress on this undamaged area will be higher than the nominal stress on total surface are and this effective stress is defined as

$$\tilde{\sigma} = \sigma \frac{dS}{dS^U} = \frac{\sigma}{1 - D} \tag{2.3}$$

where $\tilde{\sigma}$ is the effective stress acting on the undamaged area. For $D > 0$, it is clear that the effective stress is always higher than the nominal stress.

2.2. Elasticity Based Damage

Damage generally occurs under the influence of the external effects such as external loading and applied displacement. The evolution of the damage variable starts when a specific limit, the elastic limit, is reached similar to plasticity (Peerlings et al., 1998).

The elastic limit surface, which is also called as loading surface or damage criterion, is characterized by the loading function f, which is defined as

$$f(\boldsymbol{\varepsilon}, \kappa) = 0 \tag{2.4}$$

where $\boldsymbol{\varepsilon}$ is the strain tensor and κ is the history variable. For strain values which satisfy $f < 0$ condition, the material behavior is totally in the elastic region and the damage variable is stationary. The damage evolution can only be possible when the limit surface is reached ($f = 0$), please see Figure 2.1.

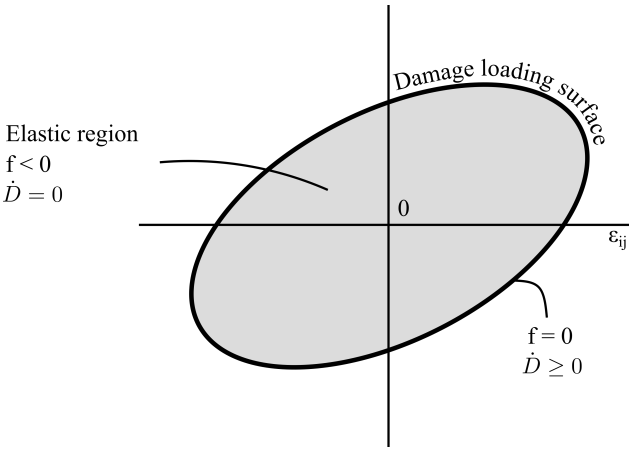

Figure 2.1. Loading surface specified in strain space

(Adopted from Peerlings, 2008)

The loading function $f(\boldsymbol{\varepsilon}, \kappa)$ for isotropic damage is given by

$$f(\boldsymbol{\varepsilon}, \kappa) = \tilde{\varepsilon}(\boldsymbol{\varepsilon}) - \kappa \tag{2.5}$$

where $\tilde{\varepsilon}$ is a scalar and equivalent measure of strain state or equivalent strain. History variable κ equals to the maximum value of the $\tilde{\varepsilon}$. If there is no damage evolution $f < 0$ condition is met and $\dot{\kappa} = 0$. As a result $f\ \dot{\kappa} = 0$ is satisfied. On the other hand, if there is damage evolution, in this case $\dot{\kappa} \geq 0$ and $f = 0$ conditions are met, since the damage

criterion reaches the surface. Because of these conditions, $f\ \dot{\kappa} = 0$ is satisfied also for this case. In a mathematical fashion, it can be said that these processes have to satisfy Karush-Kuhn-Tucker conditions which are written as

$$f\dot{\kappa} = 0 \qquad f \leq 0 \qquad \dot{\kappa} \geq 0 \tag{2.6}$$

They basically dictate that the increase of the field variable κ is positive and the damage criterion cannot be exceeded. Damage evolution can be conveniently expressed as a function of field variable κ.

$$D = D(\kappa) \tag{2.7}$$

With the help of the total form which is represented in Equation 2.7 damage evolution can also be defined in the following rate form

$$\dot{D} = g(D, \kappa)\dot{\kappa} \tag{2.8}$$

where $g(D, \kappa)$ is an arbitrary function.

2.3. Softening

In the linear elastic context, the stress-strain law is written as follows

$$\boldsymbol{\sigma} = (1 - D)\,\mathbb{C}\ : \boldsymbol{\varepsilon} \tag{2.9}$$

It is beneficial to pursue the material behavior of this constitutive model in case of a uniform, uniaxial tensile stress state $\boldsymbol{\sigma} = \sigma \boldsymbol{e_1} \otimes \boldsymbol{e_1}$, where $\boldsymbol{e_1}$ unit vector gives the direction

of the stress. It is assumed that the equivalent strain $\tilde{\varepsilon}$ is equal to the uniaxial strain ε and it is written as $\tilde{\varepsilon} = \varepsilon$ (Peerlings et al., 1998).

The differences between elasto-plasticity and damage are shown in Figure 2.2. The responses are both linear elastic at the beginning stage and they have a slope with undamaged elasticity modulus E. When the equivalent strain exceeds the threshold value κ_0 of the field variable κ, damage starts to evolve. This causes a reduction on initial slope of the response. At one point, strain softening, which means that stresses decrease with increased strains, starts. This turning point is called as limit point or snap-through point.

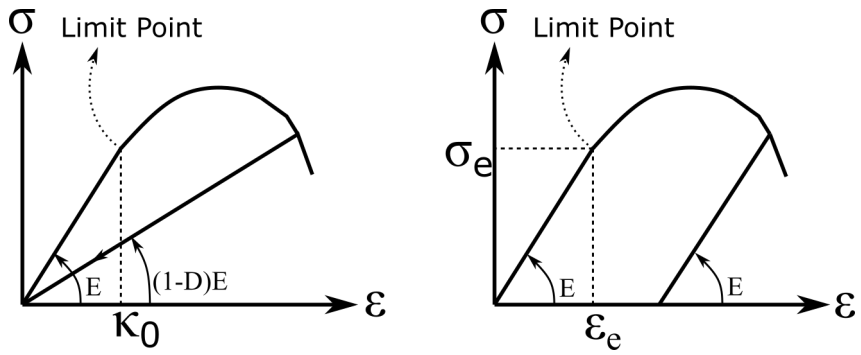

Figure 2.2. Stress-strain responses for the damage modelling and elasto-plasticity

(Adopted from Peerlings, 2008)

A similar stress-strain response can be provided by using elasto-plasticity and can be seen from the right diagram of Figure 2.2. Although the behaviors look similar at first sight, there are obvious differences between these responses especially for the unloading stages. Elasto-plastic behavior shows linear elastic unloading with a slope of virgin elasticity modulus E. Significant amount of inelastic strain still exists when the stress reaches to zero upon unloading in elasto-plastic behavior. However, in the damage model unloading reaches to zero with a decreased slope, which is equal to $(1 - D)E$, (i.e. decreased stiffness) namely secant stiffness. Since Equation 2.9 gives zero stress for zero strain, there is no inelastic deformation at the end of the unloading stage.

2.4. Mesh Dependency

Even though estimation of softening behavior with the help of continuum theories look mathematically solid and physically meaningful at the beginning, it turns out that they are not well suited (Pietruszczak and Mróz, 1981; Bažant et al., 1984). When discretized in its original form, the solution does not converge to a physically meaningful result upon mesh refinement. This phenomenon is commonly called as mesh dependency, pathological mesh sensitivity or mesh sensitivity. Previously mentioned classical continuum theories result physically unforeseen localization, which condenses all deterioration on a vanishing volume.

One dimensional setup can be used to get a deeper understanding of shortcomings of the continuum theory. For this purpose, the model represented in Figure 2.3 will be examined. The bar has mildly varying cross-sectional area $A(x)$. Similar to the mentioned example in the Section 2.3, it makes sense to assume that the equivalent strain $\tilde{\varepsilon}(x)$ is equal to the axial stress $\varepsilon(x)$. Also, the previously examined constitutive relation in Section 2.3 is used for this example.

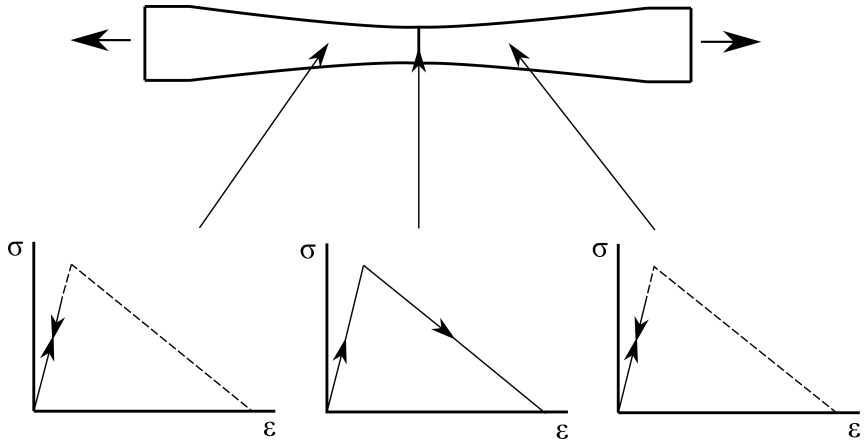

Figure 2.3. Localization of the damage along the bar

(Adopted from Peerlings, 2008)

While the bar is subjected to a tensile load of F, every cross-section along the longitudinal axis has to transfer this tensile force. Therefore, the stress σ along the bar is expressed as $\sigma(x) = F/A(x)$. The axial strain and equivalent strain are specified as $\varepsilon(x) = \tilde{\varepsilon}(x) = \sigma(x)/E$. When the threshold value of κ_0 has been reached, damage

evolution begins. Since, the smallest cross-section is located in the midspan, damage evolution starts at this point and this cross-section enters the post-peak softening region. In order to satisfy equilibrium, the stress values of neighborhood areas located slightly left and right of the midspan shall decrease. In these parts threshold values has not been reached and therefore this regions show elastic unloading response, see Figure 2.3.

If the discretization of the bar shown in Figure 2.3 is considered, only the element located at smallest cross-section enters softening branch and all of the other elements remain in elastic region and exhibit linear elastic unloading. This situation is shown in Figure 2.4. The parameter h in the figure represents the element size. For greater h values, width of the damage zone increases and amount of dissipated energy is relatively large. On the other hand, for smaller h values, the element size and width of the damaged zone decrease as well as amount of dissipated energy. In the limit case, $h \rightarrow 0$, FEM result gives coincident loading and unloading paths. It is obvious that the converged solution is not physically meaningful. This phenomenon is called as pathological mesh dependency or mesh sensitivity.

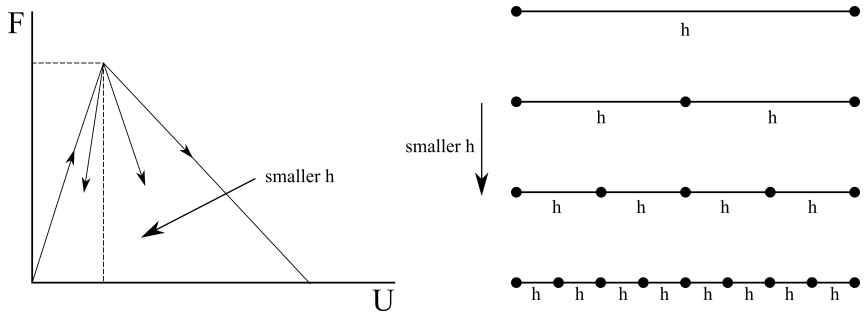

Figure 2.4. F versus U graph for different element size h

(Adopted from Peerlings, 2008)

2.5. Non-local Damage Mechanics

As seen in the previous sections, numerical solutions based on continuum damage theory converge to physically incorrect solution upon mesh refinement. To solve this issue, non-local approaches were proposed in the literature (Bažant et al., 1984; Jirásek, 1998; Peerlings et al., 1998). It is to be noted that non-local models have a smoothing

effect on the deformation and damage distribution. With the aid of the smoothing effect, localization of the damage into a small volume is prevented (Bažant et al., 1984).

Integral and gradient type non-local approaches will be summarized briefly. Then localizing implicit gradient damage model, which is used to construct two field FE formulation of this thesis, will be explained.

2.5.1. Integral Type Non-local Damage

The evolution of damage is expressed as a function of equivalent strain in Section 2.2. In integral type non-local damage models, the equivalent strain at a material point is replaced by an average value called as non-local equivalent strain, $\bar{\varepsilon}$.

On R^3, the non-local equivalent strain $\bar{\varepsilon}$ is defined for a specific point $\vec{x}$ as

$$\bar{\varepsilon}(\vec{x}) = \int_{R^3} \psi_0(\vec{x}, \vec{y})\, \tilde{\varepsilon}(\vec{y})\, dV(\vec{y}) \tag{2.10}$$

where $dV(\vec{y})$ is infinitesimal volume at $\vec{y} \in R^3$. The relation between the equivalent strain $\tilde{\varepsilon}$ and the non-local equivalent strain $\bar{\varepsilon}$ at this point is represented with the weight function $\psi_0(\vec{x}, \vec{y})$. Gauss distribution is the frequently used definition for $\psi_0(\vec{x}, \vec{y})$ and in three dimensions it can be written as

$$\psi_0(\vec{x}, \vec{y}) = \frac{1}{(2\pi)^{2/3} l_c^3} exp\left[-\frac{\xi^2}{2l_c^2}\right] \tag{2.11}$$

where $\xi = ||\vec{x} - \vec{y}||$ is the distance between points $\vec{x}$ and $\vec{y}$ and function is only dependent on this term. An important property of the weight function is specified as

$$\int_{R^3} \psi_0(\vec{x}, \vec{y})\, dV(\vec{y}) = 1 \tag{2.12}$$

It can be clearly seen that mutual effects between the points decrease with increasing distance. The l_c parameter is generally called as internal length scale and governs

the range of averaging domain. The integral length scale parameter also identifies the smoothness of strain and damage fields. In integral type non-local damage, damage and crack propagation is controlled by a finite volume despite an infinitesimal volume which is considered in local theory. The length scale parameter, l_c, should be defined by considering the microstructural properties of the material such as average grain size or particle spacing.

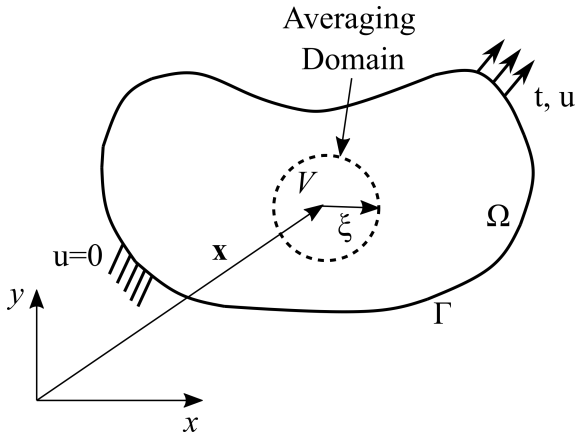

Figure 2.5. A schematic representation of non-local averaging along with the definition of averaging domain

(Adopted from Sarkar et al., 2019)

Some disadvantages of integral type non-local damage can be listed as follows. For the material points which are close to the boundaries, a considerable part of the weight function falls outside of the problem domain V. The outside parts do not participate to the integral that computes $\bar{\varepsilon}$, since the equivalent strain $\tilde{\varepsilon}$ is not defined outside of the problem domain. Non-local equivalent strain $\bar{\varepsilon}$ tends to decrease near the boundaries. A similar difficulty arises in case of internal geometric discontinuities such as notches.

2.5.2. Gradient Type Non-local Damage

In spite of defining non-local equivalent strains by using finite sized integrals, non-locality can also be introduced by using an equivalent strain and its gradient at a material point. Similar to the integral type non-local damage enhancement, an averaging domain is also used in this approach. However, gradient type non-local damage approach aims

to solve the integral operation in Equation 2.10 by using a differential approximation. With the aid of this approach, the governing equations become differential ones instead of integro-differential equations. There are at least two different formulations namely explicit and implicit gradient formulations in this approach (Peerlings et al., 1998).

To construct both implicit and explicit gradient damage formulations, $\tilde{\varepsilon}(\vec{y})$ in Equation 2.10 is first expanded as a Taylor series and the expanded form is substituted to Equation 2.10. By using Equation 2.12 it is possible to rewrite Equation 2.10 as

$$\bar{\varepsilon}(\vec{x}) = \tilde{\varepsilon}(\vec{x}) + \frac{1}{2} l_c^2 \nabla^2 \tilde{\varepsilon}(\vec{x}) + \frac{1}{8} l_c^4 \nabla^4 \tilde{\varepsilon}(\vec{x}) + \cdots \tag{2.13}$$

where $\nabla^2 = \nabla.\nabla$ is the Laplacian operator, $\nabla^4 = \nabla^2\nabla^2$ and the l_c is the internal length scale. Odd numbered coefficients of gradients disappear because of the isotropy of the weight function ψ. By considering the second order Taylor series expansion, the explicit form is expressed as

$$\bar{\varepsilon} = \tilde{\varepsilon} + \frac{1}{2} l_c^2 \nabla^2 \tilde{\varepsilon} \tag{2.14}$$

In order to get the implicit form, it is necessary to make small mathematical manipulations to Equation 2.13 before truncating it. Implicit form can be derived by taking Laplacian of Equation 2.13 and multiplying it by $\frac{1}{2} l_c^2$ and subtracting the resulting equation from Equation 2.13 which yields

$$\bar{\varepsilon} - \frac{1}{2} l_c^2 \nabla^2 \bar{\varepsilon} = \tilde{\varepsilon} + \frac{1}{8} l_c^4 \nabla^4 \tilde{\varepsilon} \tag{2.15}$$

By neglecting the second term on the right hand side, final form of implicit gradient formulation is obtained as

$$\bar{\varepsilon} - \frac{1}{2} l_c^2 \nabla^2 \bar{\varepsilon} = \tilde{\varepsilon} \tag{2.16}$$

It is clear that in implicit form, non-local equivalent strain $\bar{\varepsilon}$ is not directly computed by using equivalent strain $\tilde{\varepsilon}$ and its gradient. On the contrary, it yields a partial differential equation for $\bar{\varepsilon}$. Equation 2.16 has to be solved with equilibrium equation in a coupled manner, because the driving term $\tilde{\varepsilon}$ in Equation 2.16 is a function of strain and in term depends on the displacements. Finite element method is suitable for solving this coupled solution. It is to be noted that the Equation 2.16 requires a proper boundary condition. In this thesis the boundary condition, which is provided by Peerlings et al., 1998, is used. This boundary condition is expressed as

$$\vec{n} \cdot \nabla \bar{\varepsilon} = 0 \tag{2.17}$$

In Figure 2.6, the evolution of damage zone obtained by the implicit gradient damage formulation is shown. As can be seen from the figure, the damaged zone is widening. This artificial widening of the damage zone is one of the problems of implicit gradient damage that was also shown by other researchers (Poh and Sun, 2017; Sarkar et al., 2019; Shedbale et al., 2021).

2.5.3. Equivalent Strain Definition

Modified von Mises definition, which is firstly proposed by de Vree et al., 1995 with a strain based approach, is considered. Modified von Mises definition rooted originally from the plasticity models of polymers that uses stress tensor invariants. It is possible to rewrite strain-based modified von Mises definition as follows

$$\tilde{\varepsilon} = \frac{k-1}{2k(1-2\nu)} I_1 + \frac{1}{2k} \sqrt{\frac{(k-1)^2}{(1-2\nu)^2} I_1^2 - \frac{12k}{(1+\nu)^2} J_2} \tag{2.18}$$

where I_1 and J_2 are the first invariant of the strain tensor $\boldsymbol{\varepsilon}$ and the second invariant of the deviatoric strain tensor $\boldsymbol{\varepsilon}'$, respectively. These quantities are defined as

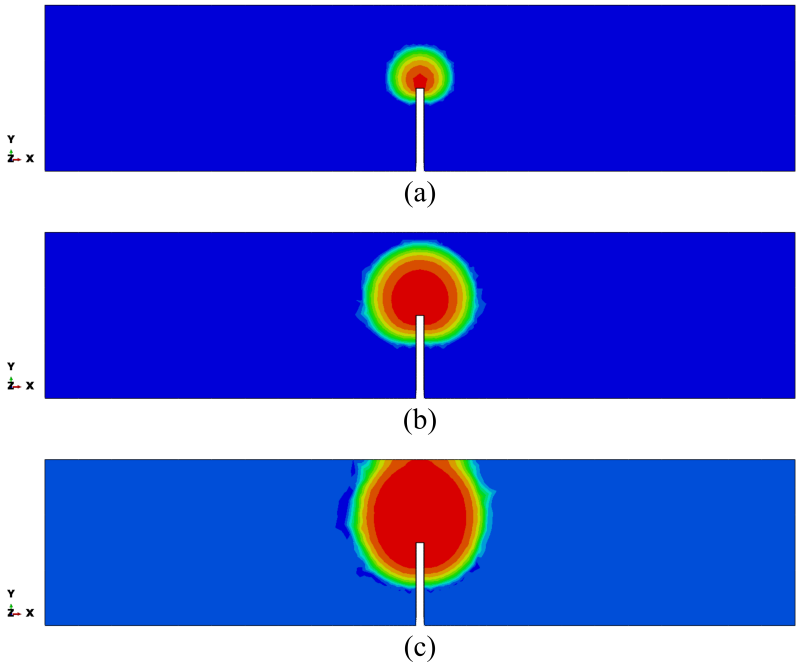

Figure 2.6. Graphical representation of the widening of damage zone during an analysis (a) Damage distribution at t=0.08s (b) Damage distribution at t=0.15 (c) Damage distribution at t=1.00s

$$I_1 = tr(\boldsymbol{\varepsilon}) \qquad J_2 = \frac{1}{6} I_1^2 - \frac{1}{2}\,\boldsymbol{\varepsilon} : \boldsymbol{\varepsilon} \tag{2.19}$$

Meaning of the parameter k is that a compressive stress $k\sigma$ has the same effect on damage evolution as a tensile stress σ. The parameter k can be written as a ratio of compressive and tensile strengths of the material; $k = \sigma_{fc}/\sigma_{ft}$.

2.5.4. Damage Evolution Law

The damage evolution law, which has a general form represented in Equation 2.7, can be considered as a measure of damage evolution in the material with respect to the strain. Exponential damage evolution law, which is used in Mazars and Pijaudier-Cabot, 1989; Brekelmans et al., 1992; de Vree et al., 1995; Peerlings et al., 1998 among others , is also used in this thesis to get a nonlinear softening response. This damage evolution

equation is expressed in the following form

$$D = \begin{cases} 0, & \text{if } \kappa \leq \kappa_0 \\ 1 - \frac{\kappa_0}{\kappa}(1 - \alpha + \alpha e^{-\beta(\kappa - \kappa_0)}), & \text{otherwise} \end{cases} \tag{2.20}$$

The damage variable converges $D = 1$ asymptotically, that means it is impossible to yield a total fracture. As $\varepsilon \to \infty$ the uniaxial stress reaches $(1 - \alpha)E\kappa_0$ and this asymptote shows the long tail of load-displacement graph.

2.6. Localizing Implicit Gradient Damage

The damage model introduced in the previous section is called as Conventional Implicit Gradient Damage (CIGD) and it has an important artificial widening of damage issue as shown in Figure 2.6. It was realized that the artificial widening of damage is rooted in fixed averaging domain (fixed interaction domain), which makes energy transfer from the damaged zone to neighboring elastically unloading regions possible, see Poh and Sun, 2017; Sarkar et al., 2019.

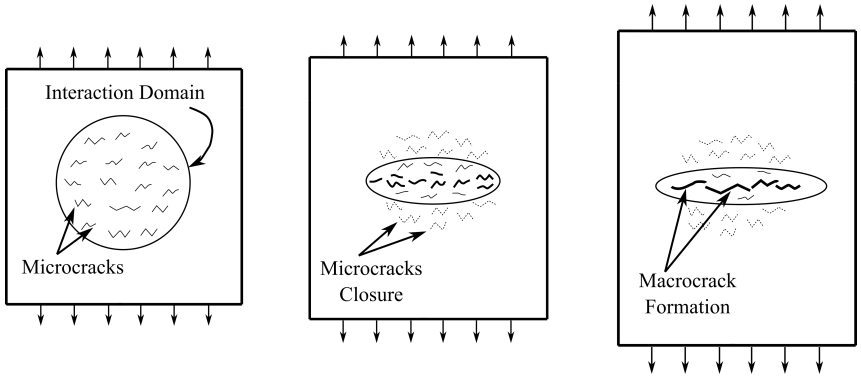

Figure 2.7. A schematic representation of non-local averaging along with the definition of averaging domain

(Adopted from Sarkar et al., 2019)

As shown in Figure 2.7, at the beginning, failure initiates with randomly located microcracks. With increased deformation, these microcracks start to grow and create

macrocracks. On the other hand with the formation of those macrocracks, the microcracks located away from the failure region are closed because of the relaxation. As a result, material failure shrinks into a smaller area. However, in CIGD the variable nature of crack propagation is ignored by using a constant averaging domain which causes spurious damage growth. Localizing Implicit Gradient Damage model (LIGD), proposed firstly in Poh and Sun, 2017, mainly aims to prevent this issue by using an evolving averaging domain. To control the size of averaging domain, an interaction function is used in LIGD.

LIGD model defines the free energy density , Ψ, as follows

$$\Psi = \frac{1}{2}(1-D)\,\boldsymbol{\varepsilon} : \mathbb{C} : \boldsymbol{\varepsilon} + \frac{1}{2}\,h\,(\tilde{\varepsilon} - \bar{\varepsilon})^2 + \frac{1}{2}\,ghl_c^2\,\nabla\bar{\varepsilon}\,\cdot\nabla\bar{\varepsilon} \tag{2.21}$$

In the Equation 2.21, the first term stands for stored elastic energy with fourth-order elasticity tensor $\mathbb{C}$ and $\boldsymbol{\varepsilon}$ is the strain tensor. The second term represents the interaction between micro and macro levels with h as coupling modulus. The equivalent strains of micro and macro levels are specified by $\tilde{\varepsilon}$ and $\bar{\varepsilon}$, respectively. Lastly, interactions of microcracks with the averaging domain are described in the third term. Similar to the CIGD, the range of the averaging domain is controlled by the internal length scale parameter, l_c. The interaction function, g, is defined to adopt interaction between microcracks during damage propagation.

By using a small h value, the residual stress existing due to coupling term during the damage evolution can be minimized. If the coupling term h is ignored, it is possible to reach a standard constitutive relation for LIGD model

$$\boldsymbol{\sigma} = (1-D)\,\mathbb{C} : \boldsymbol{\varepsilon} \tag{2.22a}$$

$$\bar{\varepsilon} - \tilde{\varepsilon} = \nabla\cdot(gl_c^2\,\nabla\bar{\varepsilon}) \tag{2.22b}$$

similar to that in Equation 2.9 of CIGD model. In fact, this modification allows a straightforward implementation of LIGD to FEM framework and it is also used in this thesis (Sarkar et al., 2019).

2.6.1. Interaction Function

According to the Poh and Sun, 2017; Sarkar et al., 2019, the interaction function g is defined as

$$g = \frac{(1 - R)\, exp(-\eta\, D) + R - exp(-\eta)}{1 - exp(-\eta)} \tag{2.23}$$

where R and η are the parameters, which govern the interaction during the damage evolution process. The material parameter η controls the evolution of g as shown on the left hand side of Figure 2.8. The other parameter R, which is called as the residual interaction parameter, defines the range of interaction as the damage reaches unity. Different interaction functions for various R values at constant η are presented on the right hand side graph of Figure 2.8. Even though, the residual interactions are completely broken at total failure in real cases, small R values are taken for numerical stability in simulations. Those parameters, R and η, are empirical and calibrated by experimental results. As illustrated in Figure 2.8, when R is taken as one, the interaction function stays constant and equals to one. Therefore, taking $R = 1$ in LIGD results in CIGD model (Sarkar et al., 2019).

2.7. Two Field Finite Element Formulation

As defined in previous sections, the constitutive relations of LIGD form a coupled system, since the driving term $\tilde{\varepsilon}$ of 2.22b is a function of strain tensor $\boldsymbol{\varepsilon}$, which depends on variable $\boldsymbol{u}$. To solve this coupled system of partial differential equations, it is necessary to construct a two field finite element formulation with independent variables displacement vector $\boldsymbol{u}$ and non-local equivalent strain $\bar{\varepsilon}$. This two field FE formulation can be constructed by starting from the balance equations with corresponding boundary conditions. These governing equations are

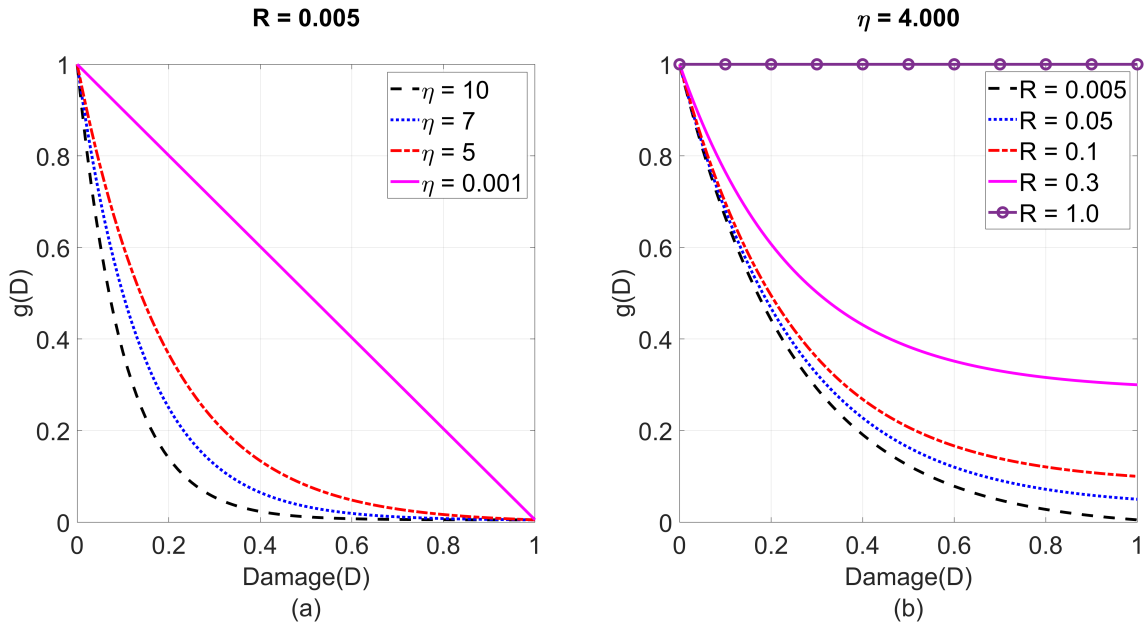

Figure 2.8. Variation of interaction function (g) with damage for (a) different values of n at $R = 0.005$, (b) different values of R at $n = 4$

$$\nabla \cdot \boldsymbol{\sigma} + \rho\, \boldsymbol{b} = \boldsymbol{0} \tag{2.24a}$$

$$\bar{\varepsilon} - \nabla \cdot (g l_c^2\, \nabla \bar{\varepsilon}) - \tilde{\varepsilon} = 0 \tag{2.24b}$$

and corresponding boundary conditions are written as follows

$$\boldsymbol{t} = \boldsymbol{\sigma} \cdot \boldsymbol{n} = \bar{\boldsymbol{t}} \quad \text{on} \quad \Gamma_t \tag{2.25a}$$

$$\boldsymbol{u} = \bar{\boldsymbol{u}} \quad \text{on} \quad \Gamma_u \tag{2.25b}$$

$$\nabla \bar{\varepsilon} \cdot \boldsymbol{n} = 0 \quad \text{on} \quad \Gamma \tag{2.25c}$$

where $\bar{\boldsymbol{u}}$ is the prescribed displacement on Γ_u and $\bar{\boldsymbol{t}}$ is the prescribed traction on Γ_t. In order to derive the weak forms of these governing equations, it is required to use two arbitrary test functions $\boldsymbol{\phi}_u$ and ϕ_ε, respectively. $\boldsymbol{\phi}_u$ has to be $\boldsymbol{\phi}_u = 0$ on Γ_u. By using

governing equations and test functions, the residual forms of governing equations for LIGD model can be expressed as follows

$$\int_V (\nabla \cdot \boldsymbol{\sigma} + \rho\, \boldsymbol{b}) \cdot \boldsymbol{\phi}_u \, dV = 0 \tag{2.26a}$$

$$\int_V \left(\bar{\varepsilon} - \nabla \cdot (g l_c^2 \, \nabla \bar{\varepsilon}) - \tilde{\varepsilon}\right) \phi_\varepsilon \, dV = 0 \tag{2.26b}$$

The expanded form of Equation 2.26a can be written as

$$\int_V \underbrace{(\nabla \cdot \boldsymbol{\sigma}) \cdot \boldsymbol{\phi}_u}_{\text{Term 1}} \, dV + \int_V \rho\, \boldsymbol{b} \cdot \boldsymbol{\phi}_u \, dV = 0 \tag{2.27}$$

It is possible to rewrite Term 1 of Equation 2.27 in an alternative way by using the following identity

$$\begin{aligned} \nabla \cdot (\boldsymbol{\sigma}\, \boldsymbol{\phi}_u) &= \nabla (\boldsymbol{\sigma}\, \boldsymbol{\phi}_u) : \boldsymbol{I} \\ \nabla \cdot (\boldsymbol{\sigma}\, \boldsymbol{\phi}_u) &= \boldsymbol{\phi}_u \cdot (\nabla \cdot \boldsymbol{\sigma}) + \nabla \boldsymbol{\phi}_u : \boldsymbol{\sigma} \\ \underbrace{\boldsymbol{\phi}_u \cdot (\nabla \cdot \boldsymbol{\sigma})}_{\text{Term 1}} &= \nabla \cdot (\boldsymbol{\sigma}\, \boldsymbol{\phi}_u) - \nabla \boldsymbol{\phi}_u : \boldsymbol{\sigma} \end{aligned} \tag{2.28}$$

Substituting this result into Equation 2.27 yields

$$\int_V \nabla \cdot (\boldsymbol{\sigma}\, \boldsymbol{\phi}_u) \; dV - \int_V \nabla \boldsymbol{\phi}_u : \boldsymbol{\sigma} \, dV + \int_V \rho\, \boldsymbol{b} \cdot \boldsymbol{\phi}_u \, dV = 0 \tag{2.29}$$

By using Gauss's divergence theorem and boundary condition, Equation 2.29 can be rewritten as

$$\int_V \boldsymbol{\sigma} : \nabla \boldsymbol{\phi}_u \, dV = \int_V \rho\, \boldsymbol{b} \cdot \boldsymbol{\phi}_u \, dV + \int_{\Gamma_t} \boldsymbol{t} \cdot \boldsymbol{\phi}_u \, dA \tag{2.30}$$

Finally, Equation 2.30 can be rewritten by using the virtual strain $\delta\boldsymbol{\varepsilon}$ as follows

$$\underbrace{\int_V \boldsymbol{\sigma} : \delta\boldsymbol{\varepsilon}\, dV}_{\substack{\text{Virtual Work done} \\ \text{by internal stresses}}} = \underbrace{\int_V \rho\, \boldsymbol{b} \cdot \boldsymbol{\phi}_u\, dV + \int_{\Gamma_t} \boldsymbol{t} \cdot \boldsymbol{\phi}_u\, dA}_{\substack{\text{Virtual Work done} \\ \text{by external forces}}} \tag{2.31}$$

where the virtual strain $\delta\,\boldsymbol{\varepsilon} = \delta\,\nabla\boldsymbol{u} = D(\nabla\boldsymbol{u})[\boldsymbol{\phi}_u] = \nabla\boldsymbol{\phi}_u$. The weak form of Equation 2.26b can be derived by using a similar approach. Firstly, the expanded form of Equation 2.26b is written as

$$\int_V \bar{\varepsilon}\, \phi_\varepsilon\, dV - g l_c^2 \int_V \underbrace{\nabla^2(\bar{\varepsilon})\, \phi_\varepsilon}_{\text{Term 2}}\, dV - \int_V \tilde{\varepsilon}\, \phi_\varepsilon\, dV = 0 \tag{2.32}$$

where, Term 2 in Equation 2.32 can be expressed as

$$\nabla^2(\bar{\varepsilon})\, \phi_\varepsilon = \nabla \cdot (\nabla\bar{\varepsilon}\, \phi_\varepsilon) - \nabla\bar{\varepsilon}\, \nabla\phi_\varepsilon \tag{2.33}$$

Therefore, by inserting Equation 2.33 into Equation 2.32 and applying Gauss's divergence theorem, the following

$$\int_V \bar{\varepsilon}\, \phi_\varepsilon\, dV - g l_c^2 \int_{\Gamma_t} \underbrace{\phi_\varepsilon\, \nabla\bar{\varepsilon} \cdot \boldsymbol{n}}_{\text{Term 3}}\, dA + g l_c^2 \int_V \nabla\bar{\varepsilon}\, \nabla\phi_\varepsilon\, dV - \int_V \tilde{\varepsilon}\, \phi_\varepsilon\, dV = 0 \tag{2.34}$$

is obtained. Term 3 in Equation 2.34 equals to zero, because of the boundary condition given in Equation 2.25c. Consequently, the weak form of the second governing equation of LIGD model takes the following form

$$\int_V \bar{\varepsilon}\, \phi_\varepsilon\, dV + g l_c^2 \int_V \nabla\bar{\varepsilon}\, \nabla\phi_\varepsilon\, dV - \int_V \tilde{\varepsilon}\, \phi_\varepsilon\, dV = 0 \tag{2.35}$$

Since the problem is nonlinear, using an incremental iterative solution is a necessity. Newton-Raphson method is going to be used for this purpose. To this end, it is required to take directional derivatives of the weak forms in the direction of the increment of independent variables. The weak forms can be written as residuals

$$r_u = \delta\, W^u_{int} - \delta\, W^u_{ext} \tag{2.36a}$$

$$r_\varepsilon = \delta\, W^\varepsilon_{int,1} + \delta\, W^\varepsilon_{int,2} - \delta\, W^\varepsilon_{ext} \tag{2.36b}$$

where r_u is the residual for the first weak form (Equation 2.31) and r_ε is the residual for the second weak form (Equation 2.35). To build a proper Newton-Raphson incremental iterative solution procedure, the above equations have to be linearized around $\boldsymbol{u}\Big|_k$ and $\bar{\varepsilon}\Big|_k$ and the following set of equations

$$r_u\Big|_k + \underbrace{D\left(r_u\right)\left[\Delta \boldsymbol{u}\right]}_{\boldsymbol{K}_{uu}\,\Delta \boldsymbol{u}} + \underbrace{D\left(r_u\right)\left[\Delta \bar{\varepsilon}\right]}_{\boldsymbol{K}_{u\varepsilon}\,\Delta \bar{\varepsilon}} = \boldsymbol{0} \tag{2.37a}$$

$$r_\varepsilon\Big|_k + \underbrace{D\left(r_\varepsilon\right)\left[\Delta \boldsymbol{u}\right]}_{\boldsymbol{K}_{\varepsilon u}\,\Delta \boldsymbol{u}} + \underbrace{D\left(r_\varepsilon\right)\left[\Delta \bar{\varepsilon}\right]}_{\boldsymbol{K}_{\varepsilon\varepsilon}\,\Delta \bar{\varepsilon}} = \boldsymbol{0} \tag{2.37b}$$

are obtained and the Newton-Raphson scheme in matrix form for this coupled nonlinear problem is given as follows

$$\begin{bmatrix} \boldsymbol{K}_{uu} & \boldsymbol{K}_{u\varepsilon} \\ \boldsymbol{K}_{\varepsilon u} & \boldsymbol{K}_{\varepsilon\varepsilon} \end{bmatrix} \begin{bmatrix} \Delta \boldsymbol{u} \\ \Delta \bar{\varepsilon} \end{bmatrix} = \begin{bmatrix} -r_u \Big|_k \\ -r_\varepsilon \Big|_k \end{bmatrix} \tag{2.38}$$

To calculate $\boldsymbol{K}_{uu}$, it is required to derive the $D\left(r_u\right)\left[\Delta \boldsymbol{u}\right]$ by following

$$D\left(r_u\right)\left[\Delta \boldsymbol{u}\right] = D\left(\delta\, W^u_{int}\right)\left[\Delta \boldsymbol{u}\right] - \underbrace{D\left(\delta\, W^u_{ext}\right)\left[\Delta \boldsymbol{u}\right]}_{\mathbf{0}}$$

$$D\left(\delta\, W^u_{int}\right)\left[\Delta \boldsymbol{u}\right] = \int_V \frac{\partial \boldsymbol{\sigma}}{\partial \boldsymbol{\varepsilon}} : D\left(\boldsymbol{\varepsilon}\right)\left[\Delta \boldsymbol{u}\right] : \delta\, \boldsymbol{\varepsilon}\; dV + \underbrace{\int_V \boldsymbol{\sigma} : D\left(\delta\, \boldsymbol{\varepsilon}\right)\left[\Delta \boldsymbol{u}\right]\; dV}_{\mathbf{0}}$$

$$\boldsymbol{K}_{uu} = D\left(r_u\right)\left[\Delta \boldsymbol{u}\right] = \int_V \mathbb{C} : \boldsymbol{A} : \delta\, \boldsymbol{\varepsilon}\; dV \tag{2.39a}$$

where $\mathbb{C} = \frac{\partial \boldsymbol{\sigma}}{\partial \boldsymbol{\varepsilon}}$ is the fourth order material tangent stiffness tensor and $\boldsymbol{A} = D\left(\boldsymbol{\varepsilon}\right)\left[\Delta \boldsymbol{u}\right] = \frac{1}{2}(\nabla(\Delta \boldsymbol{u}) + (\nabla(\Delta \boldsymbol{u}))^T)$ is a second order tensor. By following a similar approach, linearization of r_u in the direction of $\Delta\bar{\varepsilon}$, $\boldsymbol{K}_{u\varepsilon}$ yields as

$$D\left(r_u\right)\left[\Delta \bar{\varepsilon}\right] = D\left(\delta\, W^u_{int}\right)\left[\Delta \bar{\varepsilon}\right] - \underbrace{D\left(\delta\, W^u_{ext}\right)\left[\Delta \bar{\varepsilon}\right]}_{\mathbf{0}}$$

$$D\left(\delta\, W^u_{int}\right)\left[\Delta \bar{\varepsilon}\right] = \int_V \frac{\partial \boldsymbol{\sigma}}{\partial \bar{\boldsymbol{\varepsilon}}}\, D\left(\bar{\boldsymbol{\varepsilon}}\right)\left[\Delta \bar{\varepsilon}\right] : \delta\, \boldsymbol{\varepsilon}\; dV + \underbrace{\int_V \boldsymbol{\sigma} : \frac{\partial \boldsymbol{\delta}\, \boldsymbol{\varepsilon}}{\partial \bar{\boldsymbol{\varepsilon}}}\; dV}_{\mathbf{0}}$$

$$\boldsymbol{K}_{u\varepsilon} = D\left(r_u\right)\left[\Delta \bar{\varepsilon}\right] = -\int_V \frac{\partial D}{\partial \kappa}\, \frac{\partial \kappa}{\partial \bar{\varepsilon}}\, \Delta\bar{\varepsilon}\, \mathbb{C} : \boldsymbol{\varepsilon} : \delta\, \boldsymbol{\varepsilon}\; dV \tag{2.40a}$$

To linearize r_ε and calculate stiffness matrices, $\boldsymbol{K}_{\varepsilon u}$ and $\boldsymbol{K}_{\varepsilon\varepsilon}$, it is required to take directional derivative of r_ε in the directions of $\Delta \boldsymbol{u}$ and $\Delta\bar{\varepsilon}$ as follows

$$D\left(r_\varepsilon\right)\left[\Delta \boldsymbol{u}\right] = \underbrace{D\left(\delta\, W^\varepsilon_{int,1}\right)\left[\Delta \boldsymbol{u}\right]}_{\mathbf{0}} + \underbrace{D\left(\delta\, W^\varepsilon_{int,2}\right)\left[\Delta \boldsymbol{u}\right]}_{\mathbf{0}} + D\left(\delta\, W^\varepsilon_{ext}\right)\left[\Delta \boldsymbol{u}\right]$$

$$D\left(\delta\, W^\varepsilon_{ext}\right)\left[\Delta \boldsymbol{u}\right] = -\int_V \frac{\partial \tilde{\varepsilon}}{\partial \boldsymbol{\varepsilon}} : \frac{\partial \boldsymbol{\varepsilon}}{\partial \boldsymbol{u}}\, D\left(\boldsymbol{u}\right)\left[\Delta \boldsymbol{u}\right]\; \phi_\varepsilon\; dV$$

$$\boldsymbol{K}_{\varepsilon u} = D\left(r_\varepsilon\right)\left[\Delta \boldsymbol{u}\right] = -\int_V \frac{\partial \tilde{\varepsilon}}{\partial \boldsymbol{\varepsilon}} : \frac{\partial \boldsymbol{\varepsilon}}{\partial \boldsymbol{u}}\, \Delta \boldsymbol{u}\, \phi_\varepsilon\; dV \tag{2.41a}$$

and by following a similar approach, linearized form of r_ε in the direction of $\Delta\bar{\varepsilon}$ is shown as

$$
\begin{aligned}
D\left(r_\varepsilon\right)\left[\Delta\bar{\varepsilon}\right] &= D\left(\delta\, W^{\varepsilon}_{int,1}\right)\left[\Delta\bar{\varepsilon}\right] + D\left(\delta\, W^{\varepsilon}_{int,2}\right)\left[\Delta\bar{\varepsilon}\right] + \underbrace{D\left(\delta\, W^{\varepsilon}_{ext}\right)\left[\Delta\bar{\varepsilon}\right]}_{\mathbf{0}} \\
D\left(\delta\, W^{\varepsilon}_{int,1}\right)\left[\Delta\bar{\varepsilon}\right] &= \int_V \frac{\partial\bar{\varepsilon}}{\partial\bar{\varepsilon}}\, D\left(\bar{\boldsymbol{\varepsilon}}\right)\left[\Delta\bar{\varepsilon}\right]\ \phi_\varepsilon\, dV \\
D\left(\delta\, W^{\varepsilon}_{int,2}\right)\left[\Delta\bar{\varepsilon}\right] &= \frac{\partial g}{\partial D}\,\frac{\partial D}{\partial \kappa}\,\frac{\partial \kappa}{\partial\bar{\varepsilon}}\, D\left(\bar{\boldsymbol{\varepsilon}}\right)\left[\Delta\bar{\varepsilon}\right]\ l_c^2 \int_V \nabla\bar{\varepsilon}\,\nabla\phi_\varepsilon\, dV \\
&\quad + g l_c^2 \int_V D\left(\nabla\bar{\varepsilon}\right)\left[\Delta\bar{\varepsilon}\right]\ \nabla\phi_\varepsilon\, dV \\
\boldsymbol{K}_{\varepsilon\varepsilon} = D\left(r_\varepsilon\right)\left[\Delta\bar{\varepsilon}\right] &= \int_V \frac{\partial\bar{\varepsilon}}{\partial\bar{\varepsilon}}\,\Delta\bar{\varepsilon}\,\phi_\varepsilon\, dV + \frac{\partial g}{\partial D}\,\frac{\partial D}{\partial \kappa}\,\frac{\partial \kappa}{\partial\bar{\varepsilon}}\,\Delta\bar{\varepsilon}\, l_c^2 \int_V \nabla\bar{\varepsilon}\,\nabla\phi_\varepsilon\, dV \\
&\quad + g l_c^2 \int_V \nabla(\nabla\bar{\varepsilon})\,\nabla\phi_\varepsilon\, dV
\end{aligned}
\tag{2.42a}
$$

Spatial discretization of these linearized forms are specified in the following chapter.

CHAPTER 3

ISOGEOMETRIC ANALYSIS FOR 3D BODIES

In this chapter, the background information related to Isogeometric Analysis for 3D Bodies is given. A 10 noded Bézier Tetrahedra element formulation (Kadapa, 2019a) that uses existing mesh generators is re-elaborated and integrated within commercial finite element software (ABAQUS) through UEL subroutine as a user defined element. The performance of the element is assessed by means of two benchmark problems with different constitutive models.

3.1. Fundamentals of Isogeometric Analysis

There are two main approaches to represent curves and surfaces in computational geometry namely implicit equations and parametric functions.

The implicit equation of a curve can be written as $f(x, y) = 0$ in the xy plane and a surface has a form of $f(x, y, z) = 0$. For example, a unit circle with a center of origin is represented by the equation $f(x, y) = x^2 + y^2 - 1 = 0$ and in three dimensional space the surface of a sphere has an equation of the form $f(x, y, z) = x^2 + y^2 + z^2 - 1 = 0$. On the other hand, in parametric form each coordinates of a point on a curve or surface is written separately as explicit functions of independent parameters

$$\boldsymbol{C}(u) = (x(u), y(u)) \qquad a \leq u \leq b \tag{3.1}$$

At the end, $\boldsymbol{C}(u)$ becomes a vector-valued function with an independent variable u. The interval $[a, b]$ is normalized and set to $[0, 1]$.

It is not easy to comment on which of the two forms described above prevails over the other. However, the parametric form is generally used in modern Computer Aided Design programs (Piegl and Tiller, 1997). Therefore, in the following sections, mainly the parametric form is going to be examined.

3.1.1. Power Basis Form

Power Basis Form is the one of the parametric form of a curve or surface. Polynomials are the most commonly used expression for functions. Although they are conceptually simple, it is necessary to underline that polynomials are not capable to demonstrate most of the curves and surfaces directly. An nth-degree power basis curve is written as below

$$\boldsymbol{C}(u) = (x(u), y(u), z(u)) = \sum_{i=0}^{n} \boldsymbol{a}_i u^i \qquad 0 \leq u \leq 1 \tag{3.2}$$

The $\boldsymbol{a}_i = (x_i, y_i, z_i)$ quantities are also vectors in the form of

$$x(u) = \sum_{i=0}^{n} x_i u^i \qquad y(u) = \sum_{i=0}^{n} y_i u^i \qquad z(u) = \sum_{i=0}^{n} z_i u^i \tag{3.3}$$

3.1.2. Bézier curves

Bézier curves are another class of parametric polynomial curves. Mathematically, the Bézier and power basis forms are equivalent. It basically means that any curve can be represented by using one form or the other. Despite of this mathematical similarity, Bézier form is superior over the power basis form in several ways for computational modelling. The Bézier form has following advantages:

- Bézier form is more natural, because it is possible to specify both start and end points of the curve. However, in power basis form, a designer can just specify the start point of the curve.
- With the help of some existing algorithms, computations for the Bézier form has less algebraic steps than the power basis form's.

- The power basis form tends to create more round-off error because of the Horner's method.

Further imformation on Bézier curves and surfaces will be given in Section 3.2.

3.1.3. B-splines

Curve and surface computations with only one polynomial or segment are generally not satisfactory to represent complex geometries such as circles, cones, ellipses, etc. Power basis and Bézier forms of computer graphic methods have some weaknesses and these can be summarized as follows:

- (n-1) degree polynomial is necessary in order to construct a Bézier curve that passes through n data points. In other words, higher degree polynomials are necessary in order to take more data points into account. However, high degree polynomials are hard to compute and are prone to numerical instability.
- Curves and surfaces with only single segment are not adequate for interactive shape design. Even though it is possible to control Bézier curves by using their control points and weights, they do not give local control and flexibility.

In order to solve these issues, using piecewise polynomials or piecewise rationals might be a good approach. Therefore, Non-Uniform Rational Basis Splines are going to be introduced in this section.

3.1.3.1. Knot Vectors

Non-Uniform Rational Basis Splines are originally rooted from B-Splines and getting a solid insight on the B-Splines is crucial for this study. In order to construct a B-Spline, a one dimensional knot vector must be defined with an ordered set of increasing parameter values,

$$\Xi = \{\xi_1, \xi_2, \cdots, \xi_{n+p+1}\} \qquad \xi_{i+1} \geq \xi_i \tag{3.4}$$

where ξ_i is the ith knot, n is the number of basis functions used to compute B-Spline curve and p is the polynomial order. Generally, the knot vectors are normalized to fit its values in a range between zero and one. Knot vector separates the parametric space into pieces generally named as "knot spans".

If the elements in the knot vector have same distance between each other, this type of knot vectors is called as uniform. (e.g. [0 1 2 3 4 5] or [0 0.5 1]). Otherwise, knot vector is defined as non-uniform. A knot vector may be open, if its first and last knots exist $p+1$ times. If the same element of a knot vector appears k times, it means that the knot vector has a multiplicity k. In B-Spline basis functions, mostly open knot vectors are used with a multiplicity $k = p+1$ at the first and last knots.

3.1.3.2. B-Spline Basis Functions

B-Spline basis functions can be computed by using a knot vector Ξ. B-Spline basis functions $\{N_{i,p}\}_{i=1}^{n}$, which are connected to the given knot vector Ξ, can be calculated recursively starting from the independent constants $(p = 0)$:

$$N_{i,0}(\xi) = \begin{cases} 1, & \text{if} \quad \xi_i \geq \xi \geq \xi_{i+1} \\ 0, & \text{otherwise} \end{cases} \tag{3.5}$$

In case of $p \geq 1$, they are given by the following formula

$$N_{i,p}(\xi) = \frac{\xi - \xi_i}{\xi_{i+p} - \xi_i} N_{i,p-1}(\xi) + \frac{\xi_{i+p+1} - \xi}{\xi_{i+p+1} - \xi_{i+1}} N_{i+1,p-1}(\xi) \tag{3.6}$$

which is called as Cox-de-Boor recursion formula (Cox, 1972; de Boor, 1972).

As an example B-Spline basis functions created by Equations 3.5 and 3.6 for $p = 3$ and $\Xi = \{0, 0, 0, 0, 0.2, 0.4, 0.6, 0.8, 1, 1, 1, 1\}$ are shown in Figure 3.1. The red squares in the figure represent the knots. Further information and efficient algorithms can be found in Piegl and Tiller, 1997.

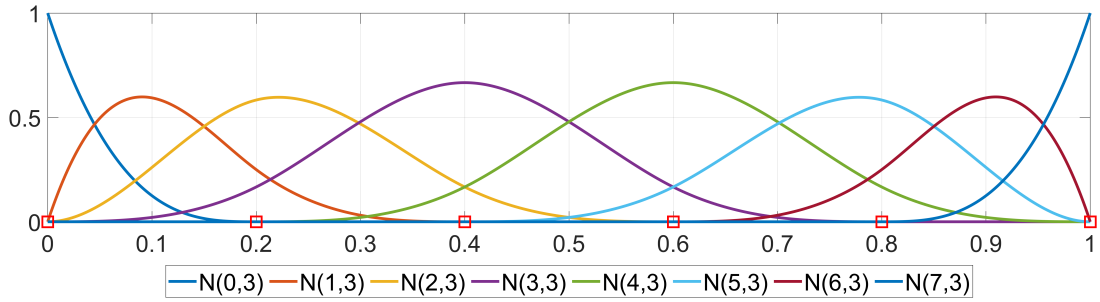

Figure 3.1. B-Spline basis functions for $p = 3$

3.1.3.3. B-Spline Curves, Surfaces and Volumes

A pth-degree B-Spline curve is specified as

$$\boldsymbol{C}(\xi) = \sum_{i=0}^{n} N_{i,p}(\xi)\boldsymbol{P}_i \tag{3.7}$$

where the $\{\boldsymbol{P}_i\}$ are the control points and the $\{N_{i,p}(\xi)\}$ are the previously mentioned B-Spline basis functions and control polygon is the polygon formed by $\{\boldsymbol{P}_i\}$. An example of a B-Spline curve with a knot vector $\Xi = \{0, 0, 0, 0, 1/4, 3/4, 1, 1, 1, 1\}$ can be seen in Figure 3.2.

The red line in Figure 3.2 is the B-Spline curve and the blue squares are the control points used to compute this curve. With a control set $\{\boldsymbol{P}_{i,j}\}$, $i = 0, 1, 2, \cdots, n-1$, $j = 0, 1, 2, \cdots, m-1$ and knot vectors $\Xi = \{\xi_1, \xi_2, \cdots, \xi_{n+p+1}\}$ and $\mathcal{H} = \{\eta_1, \eta_2, \cdots, \eta_{n+q+1}\}$ a tensor product B-Spline surface is defined as

$$\boldsymbol{S}(\xi, \eta) = \sum_{i=0}^{n}\sum_{j=0}^{m} N_{i,p}(\xi)M_{j,q}(\eta)\boldsymbol{P}_{i,j} \tag{3.8}$$

where $\{N_{i,p}(\xi)\}$ and $\{M_{j,q}(\eta)\}$ are the univariate B-spline basis functions of order p and q corresponding to knot vectors Ξ and $\mathcal{H}$. By introducing a global index as $A = n(j-1)+i$. Equation 3.8 can be fitted into the following compact form

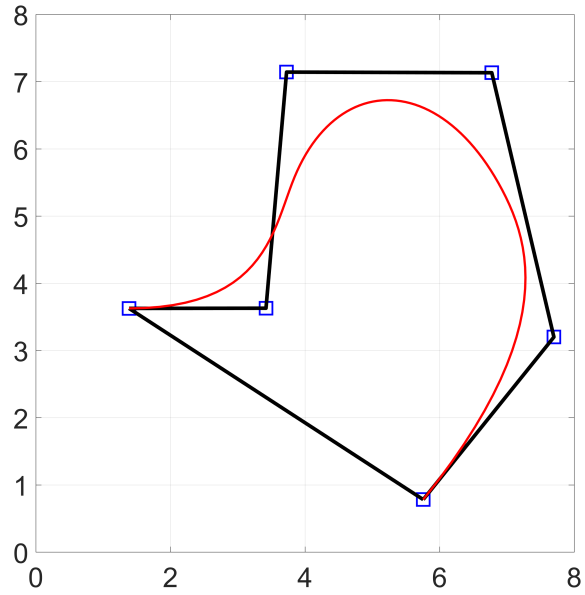

Figure 3.2. A cubic B-Spline curve, its control points and control polygon

$$\boldsymbol{S}(\boldsymbol{\xi}) = \sum_{A=0}^{n} \boldsymbol{P}_A N_A^{p,q}(\boldsymbol{\xi}) \tag{3.9}$$

where $N_A^{p,q}$ is the bivariate B-Spline basis function computed as $N_A^{p,q} = N_{i,p}(\xi)M_{j,q}(\eta)$. It is a trivial procedure to create B-Spline volumes, which are the trivariate basis defined by a tensor product of B-Spline basis functions as

$$\boldsymbol{V}(\xi,\eta,\zeta) = \sum_{i=0}^{n}\sum_{j=0}^{m}\sum_{k=0}^{l} N_{i,p}(\xi)M_{j,q}L_{k,r}(\zeta)\boldsymbol{P}_{i,j,k} \tag{3.10}$$

It is to be noted that even though there are definitions for the B-Spline and NURBS volumes, their usage is rare in CAD. CAD representations for volumes are generally composed of surface models representing the boundaries of object. For an example of a bivariate B-Spline basis function set with polynomial degrees $p = 2$ and $q = 2$ and knot vectors $\Xi = \{0,0,0,1,1,1\}$ and $\mathcal{H} = \{0,0,0,1,1,1\}$, please see Figure 3.3.

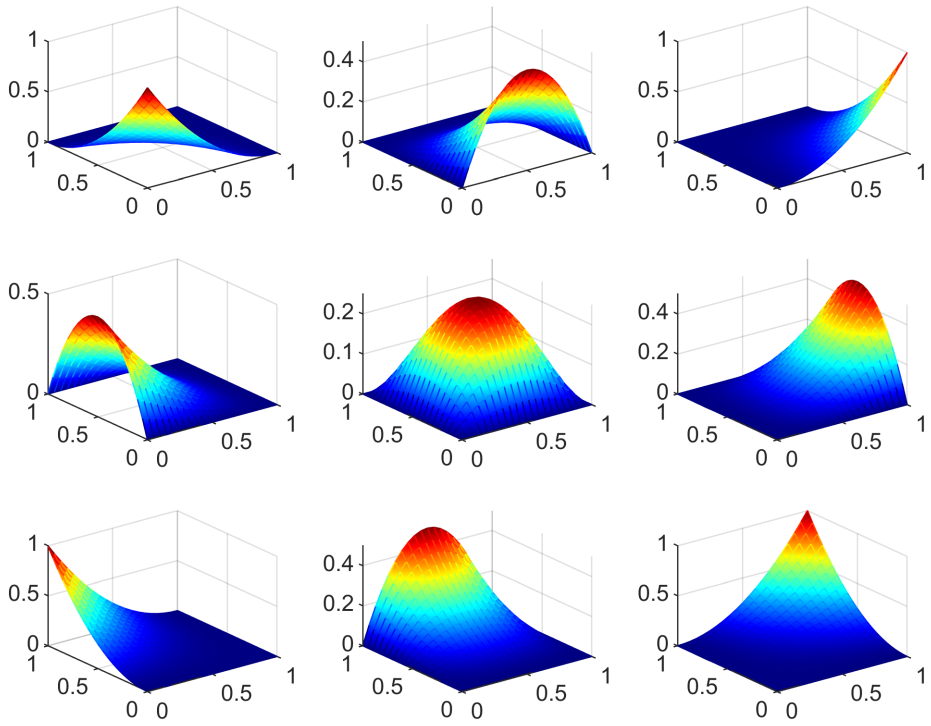

Figure 3.3. Quadratic Bivariate B-Spline basis functions

3.1.4. Non-Uniform Rational Basis Splines

B-Splines are suitable to make free-form modeling, however they are also inadequate to exactly represent some basic shapes such as circles and ellipsoids. Because of this, a generalized form of B-Spline basis called as Non-Uniform Rational Basis Splines (NURBS) has become almost a standard technology in CAD. NURBS are described through rational functions of B-Splines and inherent all the efficient properties of B-Splines. Furthermore, through NURBS, conic sections such as spheres, ellipsoids, paraboloids and hyperboloids can be exactly represented.

3.1.4.1. NURBS Basis Functions

The basis functions of NURBS are specified as

$$R_{i,p}(\xi) = \frac{N_{i,p}(\xi)w_i}{W(\xi)} = \frac{N_{i,p}(\xi)w_i}{\sum_{j=0}^{n} N_{j,p}(\xi)w_j} \tag{3.11}$$

where $\{N_{i,p}\}_{i=0}^{n}$ is the set of B-Spline basis function of order p and $\{w_i\}_{i=0}^{n}$, $w_i > 0$ is the set of NURBS weights. Utilizing proper weights allows the representation of any type of curves, not only polynomials but also circular arcs. In the particular case of equal weights, the NURBS basis reduces to the B-Spline basis. The NURBS knot vectors and weights are granted for some basic geometries in Piegl and Tiller, 1997, however, the general approach is to take these quantities from CAD tools such as Rhino with the help of user defined subroutines.

3.1.4.2. NURBS Curves, Surfaces and Volumes

The NURBS curves are introduced in a similar manner to B-Spline curves with a set of control points $\{\boldsymbol{P}_i\}$, set of weights $\{w_i\}$ and associated rational basis functions $\{R_{i,p}(\xi)\}$. They are piecewise rational functions on $\xi \in [0, 1]$ and written as

$$\boldsymbol{C}(\xi) = \sum_{i=0}^{n} R_{i,p}(\xi)\boldsymbol{P}_i \tag{3.12}$$

NURBS surfaces are computed by using the linear combinations of bivariate NURBS basis functions as

$$\boldsymbol{S}(\xi, \eta) = \sum_{i=0}^{n}\sum_{j=0}^{m} R_{i,j}^{p,q}(\xi, \eta)\boldsymbol{P}_{i,j} \tag{3.13}$$

where $\{\boldsymbol{P}_{i,j}\}$ is the set of control points and $\left\{R_{i,j}^{p,q}(\xi, \eta)\right\}$ is the bivariate NURBS basis functions with the degrees of p and q. Bivariate NURBS basis functions are specified as

$$R_{i,j}^{p,q}(\xi,\eta) = \frac{N_{i,p}(\xi)M_{j,q}(\eta)w_{i,j}}{\sum_{k=0}^{n}\sum_{l=0}^{m} N_{k,p}(\xi)M_{l,q}(\eta)w_{k,l}} \tag{3.14}$$

In a similar fashion to B-Spline volumes, NURBS volumes are structured from control points $\{\boldsymbol{P}_{i,j,k}\}$ and weights $w_{i,j,k} > 0$ as

$$\boldsymbol{V}(\xi,\eta,\zeta) = \sum_{i=0}^{n}\sum_{j=0}^{m}\sum_{k=0}^{l} R_{i,j,k}^{p,q,r}(\xi,\eta,\zeta)\boldsymbol{P}_{i,j,k} \tag{3.15}$$

where the trivariate NURBS basis functions $R_{i,j,k}^{p,q,r}$ are defined as

$$R_{i,j,k}^{p,q,r}(\xi,\eta,\zeta) = \frac{N_{i,p}(\xi)M_{j,q}(\eta)P_{k,r}(\zeta)w_{i,j,k}}{\sum_{k=0}^{n}\sum_{l=0}^{m}\sum_{s=0}^{t} N_{k,p}(\xi)M_{l,q}(\eta)P_{s,r}(\zeta)w_{k,l,s}} \tag{3.16}$$

3.1.5. Isogeometric Element Formulation

In isoparametric Finite Element Analysis (FEA) there are essentially two spaces, namely physical space and isoparametric space. In the physical space the problem domain is discretized by non-overlapping elements and corresponding representation of an element in isoparametric space is called as the parent element. In contrast to the conventional finite element formulation, there are three relevant spaces in isogeometric element formulation and these are introduced in what follows.

The first space is called as index space and it means the whole space which is specified by the knot vectors. For example, in order to demonstrate a NURBS surface, bivariate NURBS basis functions constructed from the following knot vectors $\Xi = \{0,0,0,1/2,1,1,1\}$ and $\mathcal{H} = \{0,0,0,1/3,2/3,1,1,1\}$ can be used. Index space which is defined by these knot vectors is shown in bottom right corner of Figure 3.4. Parametric space is defined by the non-zero intervals in knot vectors. For given knot vectors, the corresponding parametric space is colored with gray and blue in Figure 3.4. Physical space is where the exact geometry is computed with aid of the basis functions and the

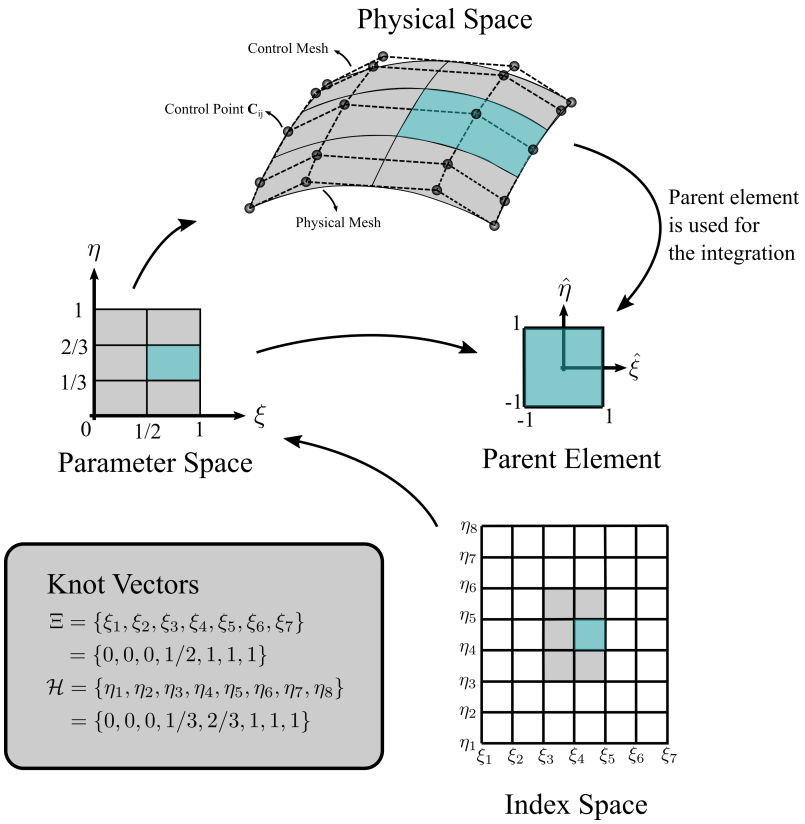

Figure 3.4. Schematic illustration of mappings in IGA for a surface model

(Adopted from Cottrell et al., 2009)

control points. An illustration of a physical space and control mesh, control points and the associated elements can be found in Figure 3.4.

The aforementioned spaces are directly related to the B-Splines and NURBS, however, an additional mapping is necessary to perform numerical integration through Gauss method. This additional space is commonly called as parent space on a domain $\widetilde{\Omega} = [-1, 1]^{d_p}$ and d_p is the problem dimension. A graphical representation of parent element can be seen in Figure 3.4. Parent space coordinates are defined as $\widetilde{\boldsymbol{\xi}} = (\widetilde{\xi}, \widetilde{\eta}, \widetilde{\zeta})$.

While constructing an isogeometric analysis formulation, three mappings are required. The first mapping is between the index space and parametric space which is easiest one and handled by just taking non-zero knot intervals. The transformation from the parent domain to a parametric domain is done by

$$
\begin{aligned}
\xi &= \frac{1}{2}\left[(\xi_{i+1} - \xi_i)\,\tilde{\xi} + (\xi_{i+1} + \xi_i)\right] \\
\eta &= \frac{1}{2}\left[(\eta_{i+1} - \eta_i)\,\tilde{\eta} + (\eta_{i+1} + \eta_i)\right] \\
\zeta &= \frac{1}{2}\left[(\zeta_{i+1} - \zeta_i)\,\tilde{\zeta} + (\zeta_{i+1} + \zeta_i)\right]
\end{aligned}
\tag{3.17}
$$

Similarly, the relation between the parametric domain and the physical domain is defined by

$$
x = \sum_{i=1}^{n} N(\boldsymbol{\xi})\,\boldsymbol{C}_i \tag{3.18}
$$

where the $N(\boldsymbol{\xi})$ represents the univariate NURBS basis function for curve, bivariate NURBS basis function for surface and trivariate NURBS basis function for solids. The control points are denoted with $\boldsymbol{C}_i$ and the number of control points is n. $\boldsymbol{\xi}$ vector collects the parametric coordinates. Jacobian of this transformation is defined by

$$
\boldsymbol{J} = \begin{bmatrix}
\dfrac{\partial x}{\partial \xi} & \dfrac{\partial x}{\partial \eta} & \dfrac{\partial x}{\partial \zeta} \\
\dfrac{\partial y}{\partial \xi} & \dfrac{\partial y}{\partial \eta} & \dfrac{\partial y}{\partial \zeta} \\
\dfrac{\partial z}{\partial \xi} & \dfrac{\partial z}{\partial \eta} & \dfrac{\partial z}{\partial \zeta}
\end{bmatrix} = \begin{bmatrix}
x_{,\xi} & x_{,\eta} & x_{,\zeta} \\
y_{,\xi} & y_{,\eta} & y_{,\zeta} \\
z_{,\xi} & z_{,\eta} & z_{,\zeta}
\end{bmatrix}
\tag{3.19}
$$

the components specified as

$$
\frac{\partial x_i}{\partial \xi_j} = \frac{\partial N_i}{\partial \xi_j}\boldsymbol{C}_{i,I} \tag{3.20}
$$

where the $\boldsymbol{C}_{i,I}$ is the ith coordinate of control point I. Finally, the spatial derivatives of NURBS basis functions with respect to coordinates of the physical domain, which is vital for element formulation both in IGA and FEA, is represented by

$$\begin{aligned}\begin{bmatrix} N_{i,x} & N_{i,x} & N_{i,z} \end{bmatrix} &= \begin{bmatrix} N_{i,\xi} & N_{i,\eta} & N_{i,\zeta} \end{bmatrix} \begin{bmatrix} \xi_{,x} & \xi_{,y} & \xi_{,z} \\ \eta_{,x} & \eta_{,y} & \eta_{,z} \\ \zeta_{,x} & \zeta_{,y} & \zeta_{,z} \end{bmatrix} \\ &= \begin{bmatrix} N_{i,\xi} & N_{i,\eta} & N_{i,\zeta} \end{bmatrix} \boldsymbol{J}_{\boldsymbol{\xi}}^{-1}\end{aligned} \tag{3.21}$$

3.2. 10-Noded Bezier Tetrahedra Element

IGA, which is introduced in the previous sections, has a potential to become an alternative to the conventional FEA. It is related not only to its ability to suppress intermediate steps between CAD model and FEA process but also its skills to represent geometries with less elements and higher exactness.

It is to be noticed that IGA requires control points and knot vectors. Although these data can be obtained from CAD programs such as Rhino, they are suitable for surface structures for example shells. For efficient analysis of 3D solid bodies on isogeometric element formulation with tetrahedral geometry is proposed by Kadapa, 2019a. By using Bernstein polynomials, a technique that makes use of existing mesh generators to construct the control points is also proposed. In the following subsections, this element is re-elaborated starting with the basic information on Bernstein polynomials.

3.2.1. Bernstein Polynomials

Bernstein polynomials (curves) are the linear combinations of Bernstein basis functions that are the special type of B-Splines and NURBS. If the weights are equal and the knot vectors contain only zeros and ones the resulting B-Splines are called as Bernstein basis functions. Trivariate Bernstein polynomials $B^n_{i,j,k,l}(\xi_1, \xi_2, \xi_3, \xi_4)$ on a tetrahedral domain are represented by the following equation

$$B^n_{i,j,k,l}(\xi_1, \xi_2, \xi_3, \xi_4) = \frac{n!}{i!j!k!l!}\xi_1^i \xi_2^j \xi_3^k \xi_4^l \qquad i+j+k+l=n \tag{3.22}$$

in terms of parametric coordinates $\xi_1, \xi_2, \xi_3, \xi_4$ where $\xi_4 = 1 - (\xi_1 + \xi_2 + \xi_3)$ and $0 \leq \xi_1, \xi_2, \xi_3, \xi_4 \leq 1$. In Equation 3.22, n represents the order of the basis function and i, j, k, l are the power of the parametric coordinates of the tetrahedral domain. Bernstein polynomials and Lagrange polynomials are coincident in cases $n = 0$ and $n = 1$. The trivariate linear ($n = 1$) Bernstein polynomials, which are used as shape functions for non-local equivalent strain field, $\bar{\varepsilon}$, are given by

$$\begin{aligned} B^1_{1000} &= N^{\varepsilon}_1 = \xi_1 \qquad & B^1_{0100} &= N^{\varepsilon}_2 = \xi_2 \\ B^1_{0010} &= N^{\varepsilon}_3 = \xi_3 \qquad & B^1_{0001} &= N^{\varepsilon}_4 = \xi_4 \end{aligned} \tag{3.23}$$

The trivariate quadratic ($n = 2$) Bernstein polynomials, which are used as shape functions of displacement field, $\boldsymbol{u}$, are written as

$$\begin{aligned} B^2_{2000} &= N_1 = \xi_1^2 \qquad & B^2_{0200} &= N_2 = \xi_2^2 \\ B^2_{0020} &= N_3 = \xi_3^2 \qquad & B^2_{0002} &= N_4 = \xi_4^2 \\ B^2_{1100} &= N_5 = 2\xi_1\xi_2 \qquad & B^2_{1010} &= N_6 = 2\xi_1\xi_3 \\ B^2_{0101} &= N_7 = 2\xi_2\xi_4 \qquad & B^2_{1001} &= N_8 = 2\xi_1\xi_4 \\ B^2_{0011} &= N_9 = 2\xi_3\xi_4 \qquad & B^2_{0110} &= N_{10} = 2\xi_2\xi_3 \end{aligned} \tag{3.24}$$

Bernstein polynomials satisfy the partition of unity

$$\sum_i^n N_i(\xi_1, \xi_2, \xi_3, \xi_4) = 1 \qquad 0 \leq \xi_1, \xi_2, \xi_3, \xi_4 \leq 1$$

and the nonnegativity

$$N_i(\xi_1, \xi_2, \xi_3, \xi_4) \geq 0 \qquad 0 \leq \xi_1, \xi_2, \xi_3, \xi_4 \leq 1$$

conditions.

Within the IGA concept, the displacement interpolation for a second order Bézier tetrahedral element requires the coordinates of the associated control points as shown in Figure 3.5.

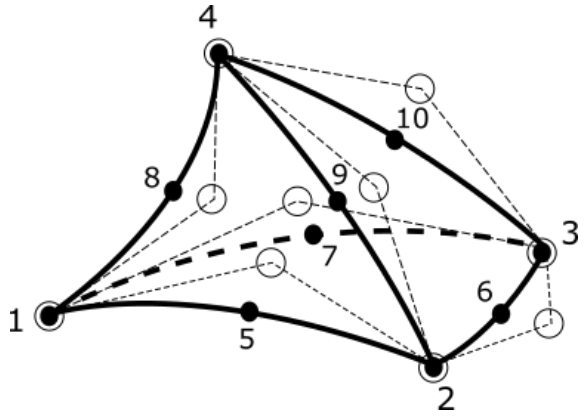

Figure 3.5. Representation of Bézier tetrahedra element (The filled circles are nodes of Lagrangian element and the circles are control points of Bézier element)

The edges of the element represented in Figure 3.5, can be considered Bézier curves and a Bézier curve is defined as a linear combination of Bernstein polynomials and related control points. Since the element is quadratic $(n = 2)$, any point on the edge between the nodes 1 and 4 in Figure 3.5 is given by

$$\boldsymbol{X}(\xi) = (1-\xi)^2\boldsymbol{P}_1 + 2\xi(1-\xi)\boldsymbol{P}_8 + \xi^2\boldsymbol{P}_4 \qquad 0 \leq \xi \leq 1 \tag{3.25}$$

where $\boldsymbol{P}_1$, $\boldsymbol{P}_4$ and $\boldsymbol{P}_8$ are the control points. It is important to note that the corner control points are interpolatory however the mid-edge control points are not. With the help of this knowledge, a straightforward mapping methodology is proposed by Kadapa, 2019a, where the control points of the quadratic Bézier tetrahedral element are computed from the nodal coordinates of the Lagrangian quadratic tetrahedral element.

$$\boldsymbol{P}_8 = \frac{1}{2\hat{\xi}(1-\hat{\xi})}\left[\boldsymbol{X}_8 - (1-\hat{\xi})^2\boldsymbol{X}_1 - \hat{\xi}^2\boldsymbol{X}_4\right] \tag{3.26}$$

If the mid-edge nodes are exactly at the middle of the edges, Equation 3.26 simplifies to

$$\boldsymbol{P}_8 = 2\left[\boldsymbol{X}_8 - 0.25\boldsymbol{X}_1 - 0.25\boldsymbol{X}_4\right] \tag{3.27}$$

Since in this case $\xi = \hat{\xi} = 0.5$, by using an analogous way and providing that the edge nodes of the Lagrange elements are exactly in the mid-edge location, it is a trivial task to extend aforementioned mapping procedure for the whole element as

$$\begin{aligned}
&\boldsymbol{P}_1 = \boldsymbol{X}_1 && \boldsymbol{P}_2 = \boldsymbol{X}_2 \\
&\boldsymbol{P}_3 = \boldsymbol{X}_3 && \boldsymbol{P}_4 = \boldsymbol{X}_4 \\
&\boldsymbol{P}_5 = 2\left[\boldsymbol{X}_5 - 0.25\boldsymbol{X}_1 - 0.25\boldsymbol{X}_2\right] && \boldsymbol{P}_6 = 2\left[\boldsymbol{X}_6 - 0.25\boldsymbol{X}_2 - 0.25\boldsymbol{X}_3\right] \\
&\boldsymbol{P}_7 = 2\left[\boldsymbol{X}_7 - 0.25\boldsymbol{X}_1 - 0.25\boldsymbol{X}_3\right] && \boldsymbol{P}_8 = 2\left[\boldsymbol{X}_8 - 0.25\boldsymbol{X}_1 - 0.25\boldsymbol{X}_4\right] \\
&\boldsymbol{P}_9 = 2\left[\boldsymbol{X}_9 - 0.25\boldsymbol{X}_2 - 0.25\boldsymbol{X}_4\right] && \boldsymbol{P}_{10} = 2\left[\boldsymbol{X}_{10} - 0.25\boldsymbol{X}_3 - 0.25\boldsymbol{X}_4\right]
\end{aligned} \tag{3.28}$$

which can be compactly written in matrix form

$$\boldsymbol{P} = \boldsymbol{L}\boldsymbol{X} \tag{3.29}$$

The explicit form of the transformation matrix $\boldsymbol{L}$ that relates control points and nodal coordinates of the Lagrangian element reads as,

$$\boldsymbol{L} = \begin{bmatrix}
1 & 0 & 0 & 0 & 0 & 0 & 0 & 0 & 0 & 0 \\
0 & 1 & 0 & 0 & 0 & 0 & 0 & 0 & 0 & 0 \\
0 & 0 & 1 & 0 & 0 & 0 & 0 & 0 & 0 & 0 \\
0 & 0 & 0 & 1 & 0 & 0 & 0 & 0 & 0 & 0 \\
-0.5 & -0.5 & 0 & 0 & 2 & 0 & 0 & 0 & 0 & 0 \\
0 & -0.5 & -0.5 & 0 & 0 & 2 & 0 & 0 & 0 & 0 \\
-0.5 & 0 & -0.5 & 0 & 0 & 0 & 2 & 0 & 0 & 0 \\
-0.5 & 0 & 0 & -0.5 & 0 & 0 & 0 & 2 & 0 & 0 \\
0 & -0.5 & 0 & -0.5 & 0 & 0 & 0 & 0 & 2 & 0 \\
0 & 0 & -0.5 & -0.5 & 0 & 0 & 0 & 0 & 0 & 2
\end{bmatrix} \tag{3.30}$$

The same mapping technique is also used for the displacement field and embedded within the standard steps of the finite element method. In other words, nodal coordinates and displacements are converted into coordinates and displacements of control points. The basic steps of this transformation algorithm are given in Algorithm 1.

Algorithm 1 Mapping between nodal and control point quantities

Convert nodal quantities to control point quantities

$$\boldsymbol{u}_c = \boldsymbol{L}\,\boldsymbol{u}_n$$

$$\boldsymbol{P} = \boldsymbol{L}\,\boldsymbol{X}$$

Calculate element internal force vector and tangent stiffness matrix in terms of control point quantities

Convert element internal force vector and tangent stiffness matrix to nodal quantities for Abaqus solver

$$\boldsymbol{F}_n^{int} = \boldsymbol{L}^T\,\boldsymbol{F}_c^{int}$$

$$\boldsymbol{K}_n = \boldsymbol{L}^T\,\boldsymbol{K}_c\,\boldsymbol{L}$$

3.2.2. Discretization

By using the introduced shape functions (Equations 3.23 and 3.24), it is possible to make spatial discretization of the weak forms, given in Equations 2.31 and 2.35. For this purpose, the independent variables $\boldsymbol{u}$ and $\bar{\varepsilon}$ are discretized by using quadratic and linear Bernstein interpolation functions respectively as

$$\boldsymbol{u} = \boldsymbol{N}\,\hat{\boldsymbol{u}} \tag{3.31a}$$

$$\bar{\varepsilon} = \boldsymbol{N}_{\varepsilon}\,\hat{\bar{\boldsymbol{\varepsilon}}} \tag{3.31b}$$

their gradients are shown as

$$\boldsymbol{\varepsilon} = \nabla\, \boldsymbol{N}\, \hat{\boldsymbol{u}} = \boldsymbol{B}\, \hat{\boldsymbol{u}} \tag{3.32a}$$

$$\nabla\, \bar{\varepsilon} = \nabla\, \boldsymbol{N}_{\varepsilon}\, \hat{\bar{\boldsymbol{\varepsilon}}} = \boldsymbol{B}_{\boldsymbol{\varepsilon}}\, \hat{\bar{\boldsymbol{\varepsilon}}} \tag{3.32b}$$

where $\hat{\boldsymbol{u}}$ and $\hat{\bar{\boldsymbol{\varepsilon}}}$ are the nodal quantities for displacement and non-local equivalent strain fields, respectively. In addition to these discretized quantities, the corresponding test functions have to be discretized as

$$\boldsymbol{\phi_u} = \boldsymbol{N}\, \hat{\boldsymbol{\phi}}_{\boldsymbol{u}} \qquad \text{and} \qquad \phi_{\varepsilon} = \boldsymbol{N}_{\boldsymbol{\varepsilon}}\, \hat{\boldsymbol{\phi}}_{\boldsymbol{\varepsilon}} \tag{3.33}$$

their gradients are written as follows

$$\nabla \boldsymbol{\phi_u} = \boldsymbol{B}\, \hat{\boldsymbol{\phi}}_{\boldsymbol{u}} \qquad \text{and} \qquad \nabla \phi_{\varepsilon} = \boldsymbol{N}_{\boldsymbol{\varepsilon}}\, \hat{\boldsymbol{\phi}}_{\boldsymbol{\varepsilon}} \tag{3.34}$$

Therefore, by substituting these discretized fields into Equations 2.31 and 2.35, the following final forms

$$\int_V \boldsymbol{B}^T\, \boldsymbol{\sigma}\, dV = \int_V \boldsymbol{N}^T\, \rho\, \boldsymbol{b}\, dV + \int_{\Gamma_t} \boldsymbol{N}^T\, \boldsymbol{t}\, dA \tag{3.35a}$$

$$\int_V \boldsymbol{N}_{\varepsilon}^T\, \bar{\varepsilon}\, dV + g l_c^2 \int_V \boldsymbol{B}_{\boldsymbol{\varepsilon}}{}^T\, \nabla \bar{\varepsilon}\, dV - \int_V \boldsymbol{N}_{\boldsymbol{\varepsilon}}{}^T\, \tilde{\varepsilon}\, dV = \boldsymbol{0} \tag{3.35b}$$

are obtained. The corresponding discretized form of linearized equations for LIGD model in matrix form read as

$$\begin{bmatrix} \boldsymbol{K}_{uu} & \boldsymbol{K}_{u\varepsilon} \\ \boldsymbol{K}_{\varepsilon u} & \boldsymbol{K}_{\varepsilon\varepsilon} \end{bmatrix} \begin{bmatrix} \Delta \boldsymbol{u} \\ \Delta \bar{\varepsilon} \end{bmatrix} = \begin{bmatrix} \boldsymbol{F}_{ext}^{u} - \boldsymbol{F}_{int}^{u} \\ -\boldsymbol{F}_{int}^{\varepsilon} \end{bmatrix} \tag{3.36}$$

where element force vectors are

$$\boldsymbol{F}^{u}_{ext} = \sum_{n=1}^{n_e} \left(\int_{V_e} \boldsymbol{N}^T \, \rho \, \boldsymbol{b} \, dV + \int_{\Gamma_t} \boldsymbol{N}^T \, \boldsymbol{t} \, dA \right) \tag{3.37a}$$

$$\boldsymbol{F}^{u}_{int} = \sum_{n=1}^{n_e} \left(\int_{V_e} \boldsymbol{B}^T \, \boldsymbol{\sigma} \, dV \right) \tag{3.37b}$$

$$\boldsymbol{F}^{\varepsilon}_{int} = \sum_{n=1}^{n_e} \left(\int_{V_e} \boldsymbol{N}^T_{\varepsilon} \, \bar{\varepsilon} \, dV + g l_c^2 \int_{V_e} \boldsymbol{B}^T_{\varepsilon} \, \nabla \bar{\varepsilon} \, dV - \int_{V_e} \boldsymbol{N}^T_{\varepsilon} \, \tilde{\varepsilon} \, dV \right) \tag{3.37c}$$

and the components of tangent stiffness matrices are specified

$$\boldsymbol{K}_{uu} = \sum_{n=1}^{n_e} \left(\int_{V_e} \boldsymbol{B}^T \, (1 - D) \, \mathbb{C} \, \boldsymbol{B} \, dV \right) \tag{3.38a}$$

$$\boldsymbol{K}_{u\varepsilon} = \sum_{n=1}^{n_e} \left(-\int_{V_e} \frac{\partial D}{\partial \kappa} \, \frac{\partial \kappa}{\partial \bar{\varepsilon}} \, \boldsymbol{N}^T_{\varepsilon} \, \mathbb{C} : \boldsymbol{\varepsilon} \, \boldsymbol{B} \, dV \right) \tag{3.38b}$$

$$\boldsymbol{K}_{\varepsilon u} = \sum_{n=1}^{n_e} \left(-\int_{V_e} \frac{\partial \tilde{\varepsilon}}{\partial \boldsymbol{\varepsilon}} : \frac{\partial \boldsymbol{\varepsilon}}{\partial \boldsymbol{u}} \, \boldsymbol{N}^T_{\varepsilon} \, \boldsymbol{B} \, dV \right) \tag{3.38c}$$

$$\begin{aligned} \boldsymbol{K}_{\varepsilon\varepsilon} = \sum_{n=1}^{n_e} \Bigg(& \int_{V_e} \boldsymbol{N}^T_{\varepsilon} \, \boldsymbol{N}_{\varepsilon} \, dV + \int_{V_e} \frac{\partial g}{\partial D} \, \frac{\partial D}{\partial \kappa} \, \frac{\partial \kappa}{\partial \bar{\varepsilon}} \, l_c^2 \, \boldsymbol{B}^T_{\varepsilon} \, \nabla \bar{\varepsilon} \, \boldsymbol{N}_{\varepsilon} \, dV \\ & + \int_{V_e} \boldsymbol{B}^T_{\varepsilon} \, g l_c^2 \, \boldsymbol{N}_{\varepsilon} \, dV \Bigg) \end{aligned} \tag{3.38d}$$

This introduced nonsymmetric stiffness matrix is implemented in incremental iterative Newton-Raphson solution procedure. As represented in Subsection 2.6.1 and shown in Figure 2.8, previously driven finite element formulation for LIGD model can be converted into the CIGD model just setting $R = 1$ in the interaction function, Equation 2.23. This modification results a constant interaction function, which is equal to one.

It is to be noted that, element integrals are evaluated by using the four-point Gauss quadrature rule.

3.2.3. Abaqus Implementation

This presented formulation is implemented in the commercial FE solver Abaqus through user defined element (UEL) subroutine, since this element formulation does not exist in the Abaqus element library. A summarized workflow for this implementation is given in Figure 3.6.

A ten noded quadratic 3D Bézier element is created. The displacement degrees of freedom (DOF) defined all nodes of the element, whereas non-local equivalent strain DOFs are defined only at the corner nodes, please see Figure 3.6. The total number of DOFs become 34 as 30 of them are related to the displacements in x-, y- and z-directions and four of them are related to the nodal non-local equivalent strain values.

The implementation of UEL subroutine can be considered under two parts: (a) Input file (*.inp) and (b) FORTRAN file (*.for). The input file includes the representative data for the analysis and FORTRAN file controls the computational model which is implemented by the user.

The input file (*.inp) has the Abaqus keywords and material properties along with the element and connectivity data for the analysis. On the other hand, FORTRAN file has the user defined element details. It is possible to divide FORTRAN file into two parts. UEL subroutine includes the necessary computational steps for calculating the element stiffness matrix and internal force column by using the aforementioned discretized constitutive relations. Finite element assembly and solution of the system of equations are performed by Abaqus.

As mentioned before, an incremental iterative solution algorithm, the Newton-Raphson method, is used to solve the coupled nonlinear system of equations. For this solution procedure, the computation of tangent stiffness at the beginning of every iteration is necessary. At the end of the analysis, an output database file (*.odb) is created by the Abaqus and that file contains the nodal quantities and solution dependent variables (SDV). There are mainly two alternatives to read and visualize the output database file. The first alternative is writing a Python script to read and visualize the output by using some visualization package. Another way of the visualization of the output database file is using the library elements of Abaqus. To achieve this, it is necessary to pass the computed data of user defined element to the Abaqus library element during the analysis.

This transfer can be done by using an Abaqus subroutine, which is called as UVARM. With the aid of this subroutine, solutions obtained from the user defined element can be visualized through Abaqus' library elements. In order to complete this transfer for each user element, a "dummy" element with the same connectivity of UEL is created. This dummy element has 10 noded tetrahedral topology and they behave elastically with the very small modulus of elasticity $(E = 1x10^{-12})$, so that they do not influence the solution. An illustrated summary of this transfer process is shown in Figure 3.6.

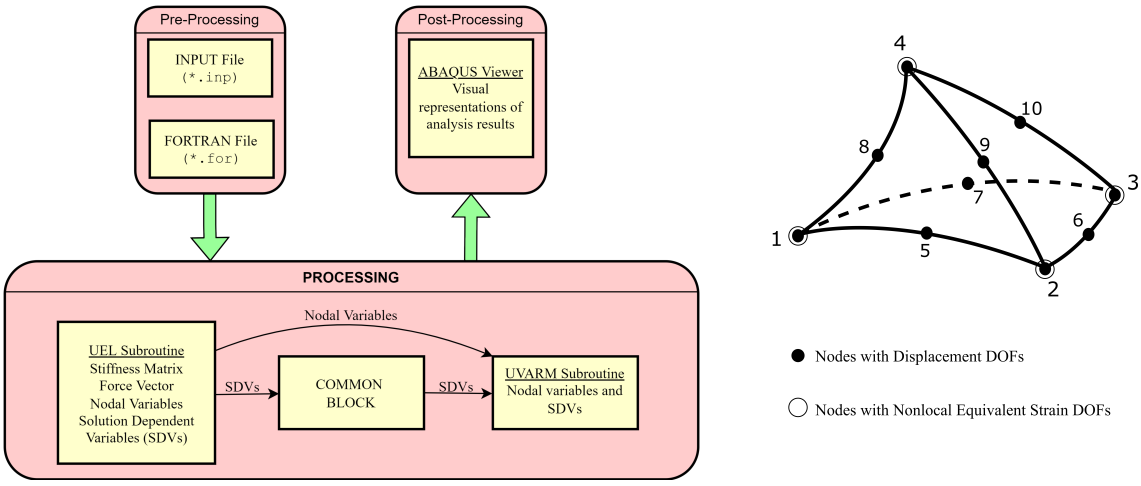

Figure 3.6. Workflow in Abaqus during the analysis through UEL subroutine and two field element with nodes

The main steps of the UEL subroutine is given in the following algorithm.

Algorithm 2 UEL Subroutine algorithm for a single element

Read $\boldsymbol{u}$ and $\bar{\varepsilon}$ values from the previous iteration

Convert nodal quantities to the control point quantities ▷ Algorithm 1

Loop over integration points starts

Calculate $\boldsymbol{\varepsilon}$

Evaluate $\tilde{\varepsilon}$, D and g ▷ Eqs. 2.18, 2.20 and 2.23

Compute $\boldsymbol{\sigma}$ ▷ Equation 2.9

Compute $\boldsymbol{F}^{u}_{ext}$, $\boldsymbol{F}^{u}_{int}$ and $\boldsymbol{F}^{\varepsilon}_{int}$ ▷ Equations 3.37

Compute $\boldsymbol{K}_{uu}$, $\boldsymbol{K}_{u\varepsilon}$, $\boldsymbol{K}_{\varepsilon u}$ and $\boldsymbol{K}_{\varepsilon\varepsilon}$ ▷ Equations 3.38

Convert the above control point quantities to the nodal quantities ▷ Algorithm 1

3.3. Numerical Examples

The implementation has to be validated by benchmark problems. Therefore, two numerical examples are considered to assess the performance of the quadratic tetrahedral Bézier element. It is to be noted that, in these benchmark problems nearly incompressible material behavior is considered and another two field element formulation ($\boldsymbol{u}$-$\boldsymbol{p}$ element) is created. For further information about nearly incompressible material behavior and two field $\boldsymbol{u}$-$\boldsymbol{p}$ formulation, please refer Bathe, 2014. The solutions obtained by hybrid hexahedra element (quadratic displacement and linear pressure interpolations, Abaqus element type C3D20H) are taken as the reference solution. To get a consistent comparison, the Abaqus element was selected as hexahedra element, since the quadratic tetrahedral Abaqus element has constant pressure interpolation.

3.3.1. 3D Tapered Beam

In this example, a tapered beam model, which is 3D version of well known 2D Cook's Membrane, is considered with nearly incompressible linear elastic material behavior. The example's geometry and the boundary conditions are taken from Kadapa, 2019a and shown in Figure 3.7.

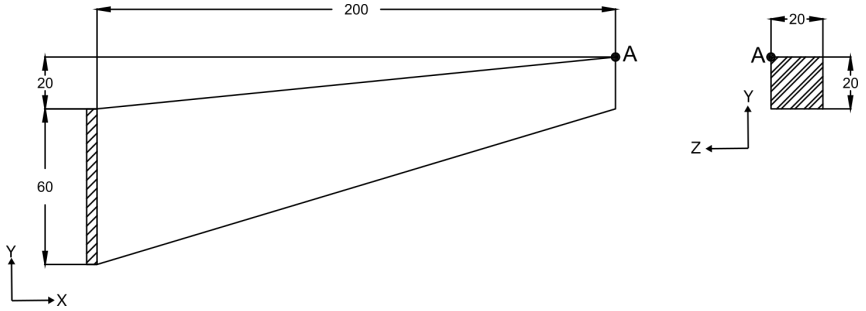

Figure 3.7. The geometry and boundary conditions of the tapered beam (units in mm)

The material properties are used as proposed in Kadapa's paper and the modulus of elasticity and Poisson's ratio are taken as, 240.565 MPa and 0.4999, respectively. The surface traction is applied to the free surface (represented as hatched area in Figure 3.7) of the beam. Magnitude of the surface traction is 2 N/mm^2 in the y-direction and 0.4

Table 3.1. Used meshes and number of elements for elastic tapered beam analysis

	Total Elements	**Total Nodes**
UEL Mesh	21242	33341
Abaqus Mesh	8192	36737

N/mm^2 in the z-direction. The displacement values in the y-direction of point A are collected to construct a convergence graph for quadratic Bézier tetrahedral element by using successively refined meshes, please see Figure 3.8. Even though the total number of elements used in UEL mesh is higher than the Abaqus mesh, the total number nodes in UEL mesh is slightly less than the Abaqus mesh. Because of this difference, sizes of the stiffness matrix and force vector are going to be smaller for mesh with tetrahedral elements.

Except the analysis with very coarse mesh, which consists only 21 elements, results obtained by using quadratic Bézier tetrahedral element are very close with the hybrid hexahedra element, please see Figure 3.8. Furthermore, a comparison between displacement of Point A and reaction force values in the y-direction at the fixed end of tapered beam is shown in Figure 3.9. The details of the used meshes are given in Table 3.1. It is to be noticed that the curves are almost coincident in Figure 3.9.

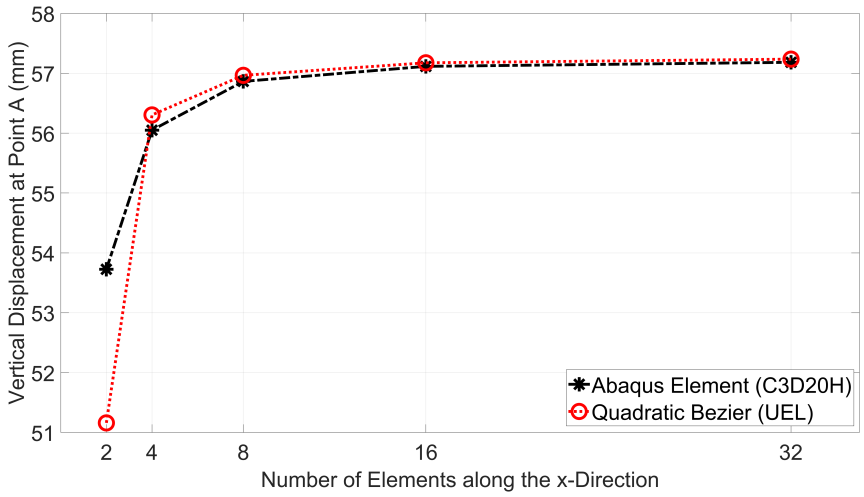

Figure 3.8. Convergence study for displacements in the y-direction of point A

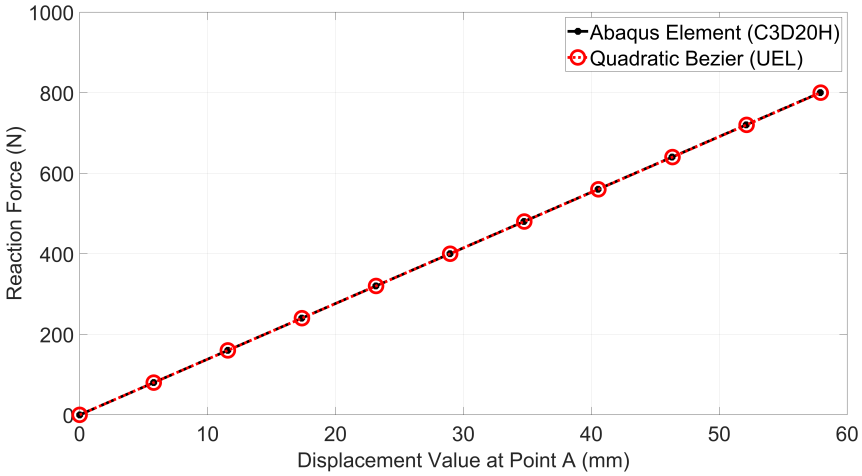

Figure 3.9. Reaction force versus displacement graph in the y-direction

3.3.2. Von Mises (J2) Plasticity Example

In the second example, a plate with a central hole under tensile loading is considered with the classical J2 plasticity model without hardening. Because of the symmetry, 1/8th of the geometry (as shown with red dashed lines in Figure 3.10) was modeled and analyzed by using the quadratic Bézier tetrahedral elements. The geometry and the boundary conditions used in the analysis can be seen in Figure 3.10.

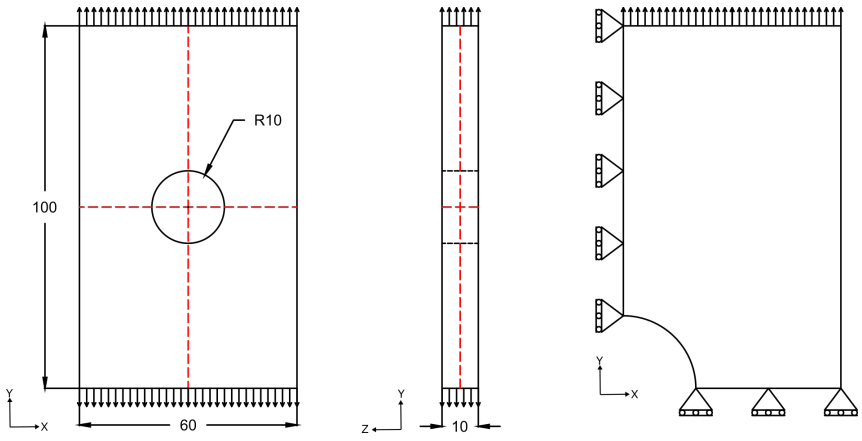

Figure 3.10. The geometry and boundary conditions of the plate with a central hole (units in mm)

The modulus of elasticity, Poisson's ratio and the yield stress are taken as 200000

MPa, 0.4999 and 600 MPa, respectively. A displacement controlled loading is applied at the top surface of the specimen which is increased linearly and reached a final value of 3-mm. The analyses are conducted using both the quadratic Bézier tetrahedra element with a mesh that contains 1213 elements and Abaqus element type C3D20H with a mesh that contains 1767 elements. The deformed shapes obtained from both of the FE analyses and vertical displacement contours are shown in Figure 3.11, the left figure is the reference solution and right is the quadratic Bézier . Reaction force components in the y-direction are collected from nodes of the top surface and summed up to plot a reaction force versus displacement graph. As can be clearly seen from Figure 3.12, the resulting force-displacement graphs are almost coincident.

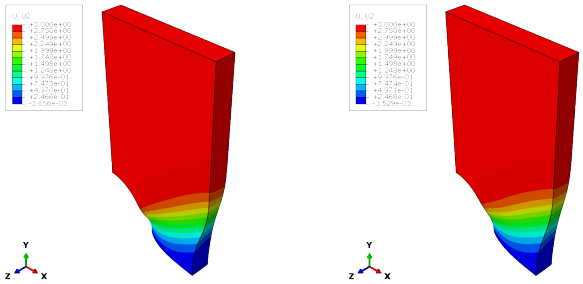

Figure 3.11. Deformed shapes for both reference element and quadratic Bézier element with vertical displacement contour

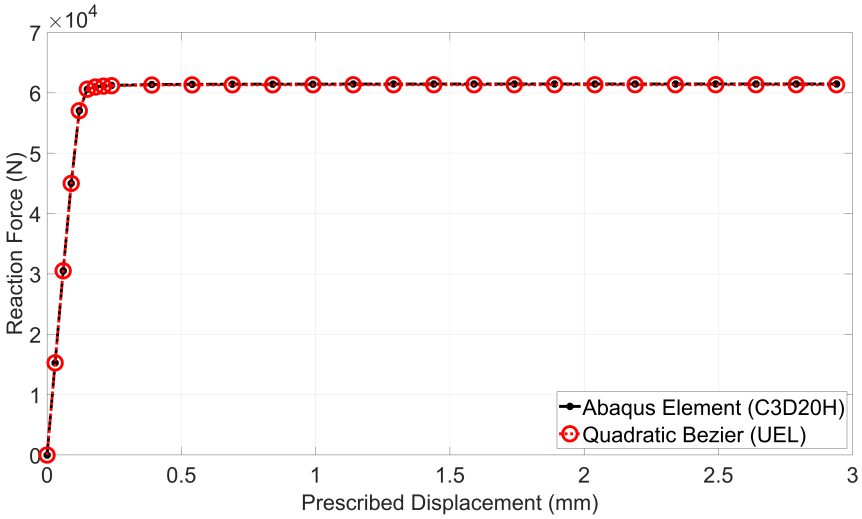

Figure 3.12. Reaction force versus displacement graph in the y-direction

CHAPTER 4

THREE DIMENSIONAL CASE STUDIES

4.1. 3 Point Bending Test

This experimental setup was proposed and a series of tests were conducted by Jefferson et al., 2004. The purpose of using this example is to examine the performance of the two field Bézier tetrahedral element in the case of planar fracture propagation.

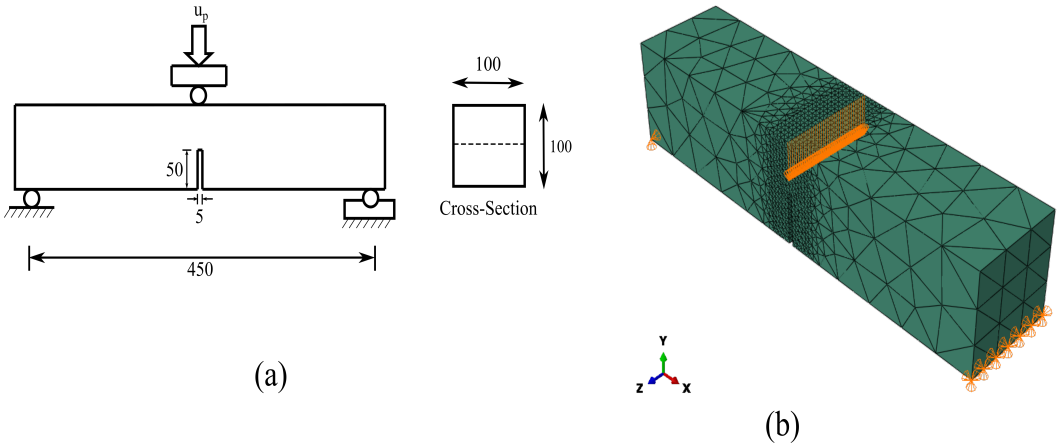

Figure 4.1. Test setup and FE model (a) Test setup with boundary conditions and dimensions (b) FE model used in the analyses (all dimensions in mm)

The test setup with its geometrical details and dimensions are presented in the left hand side of Figure 4.1. The test specimen is 100 mm x 100 mm in cross-section and 450 mm in length. The notch is located in the midspan and it has a depth of 50 mm and a width of 5 mm. In a displacement controlled setting, the prescribed displacement is applied and distributed along the depth by means of a cylindrical steel mill as shown in Figure 4.1. The FE model with boundary conditions can be seen in the right hand side.

For this example, both CIGD and LIGD models were considered and used in the analyses. Material properties used in this example are given in Table 4.1.

Table 4.1. Used parameters for three point bending test

$E(N/mm^2)$	ν	R	n	β	κ_0	α	l_c	k
35000	0.2	0.005	1	85	9.00E-05	0.96	2	13.9

Table 4.2. Used meshes and number of elements for three point bending test

	Total Elements
Mesh #1	13539
Mesh #2	21024
Mesh #3	33775
Mesh #4	43409

In order to carry out a mesh convergence study, four analyses with different number of elements were done. The details of the used meshes are given in Table 4.2. After completion of these analyses, the prescribed vertical displacement values and the corresponding reaction force values were collected. The corresponding displacement versus force graphs can be seen in Figure 4.2.

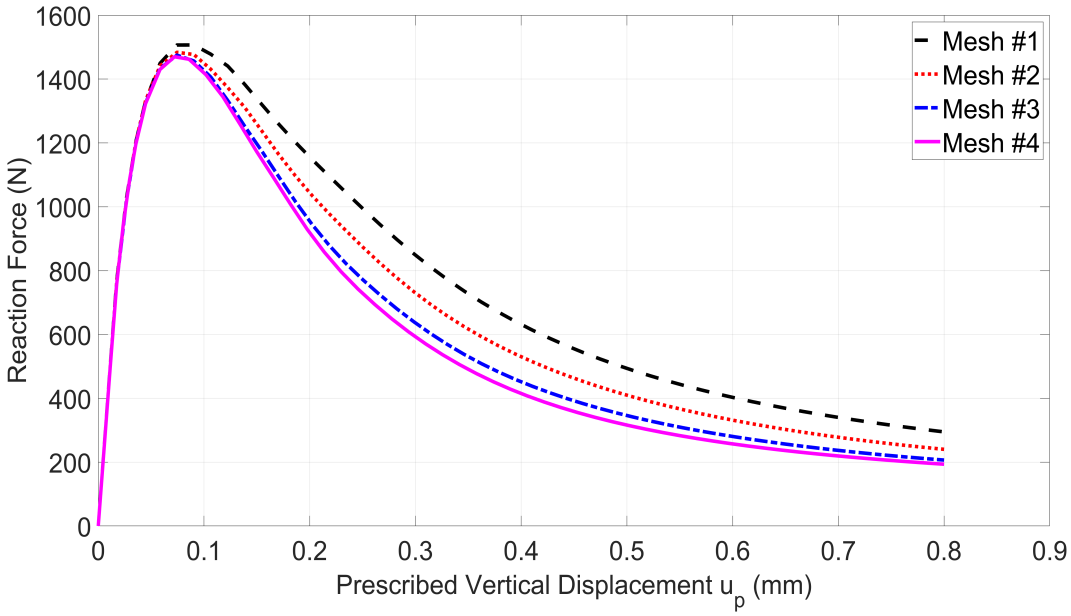

Figure 4.2. Results of mesh convergence study for three point bending test

The fourth mesh was selected for further investigations and comparisons with solutions from Jefferson et al., 2004. The comparison between the experimental and numerical predictions of other studies and FEA results of the current study can be seen in Figure 4.3.

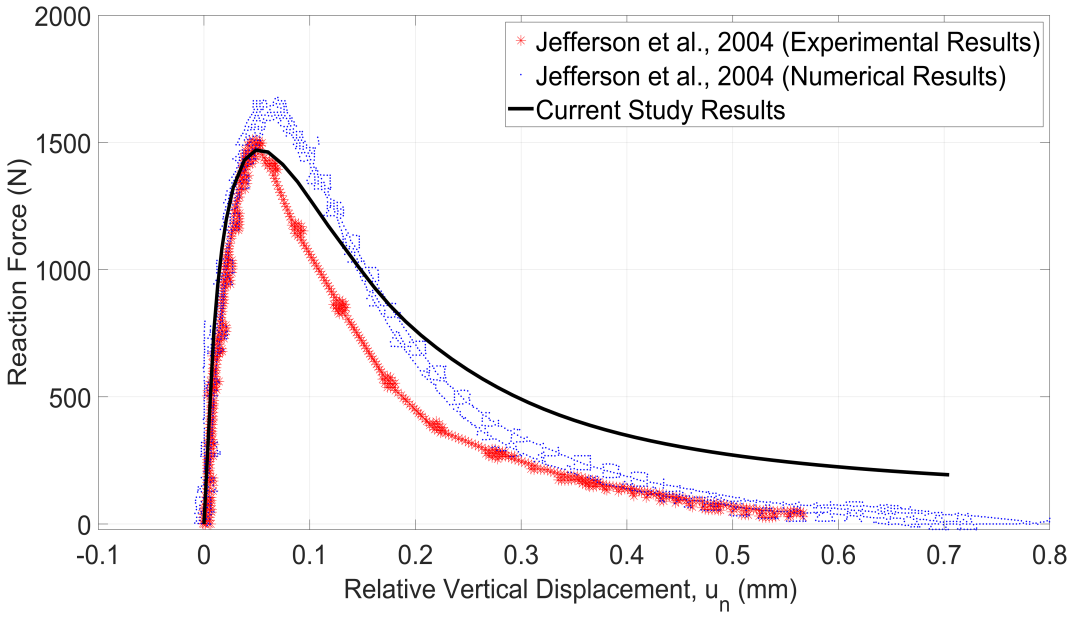

Figure 4.3. Comparison of experimental and numerical results for prescribed displacements (u_n) versus reaction force values in three point bending test

Result for the continuum damage model, which is described in a detailed fashion in the previous sections, is shown with black line and experimental results are represented with red stars and blue dots in Figure 4.3. It can be stated that, peak force prediction of the FE analysis looks sufficient (the values of FE result and the average of experimental results are 1469.9N and 1511.8N, respectively and the difference is around 2.8%). In the post peak regime the FE analysis result falls higher than the experimental and numerical results of Jefferson et al., 2004 almost throughout the loading history.

The deformed shape obtained from the FE analysis with vertical displacement contour is located in the left hand side of Figure 4.4. The Gauss quadrature point locations with a damage variable of $d \geq 0.99$ and their coordinates were gathered. These coordinate points and the border of the analyzed model were plotted to make a visual representation of the crack surface around the notch. The planar behavior of the crack surface is clearly visible in the right hand side of Figure 4.4.

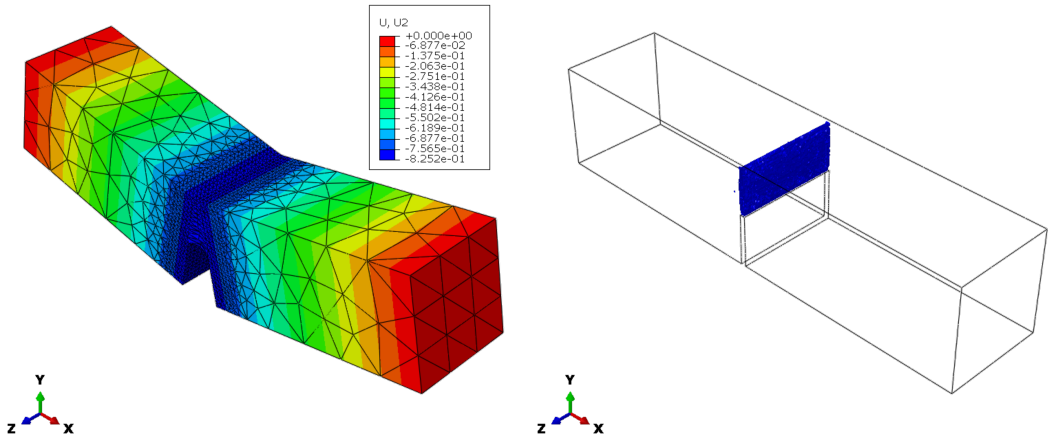

(a) (b)

Figure 4.4. Analysis results (a) Deformed shape with vertical displacement contour (with a scaling factor of 50) (b) Isometric view of fracture surface

In Figure 4.5, the views (a) and (b) show the damage contours of the current study obtained by using LIGD and CIGD models. In view (b) it is clearly seen that the damage zone diffuses to a wide band. It is difficult to identify a sharp fracture surface. Whereas, in the case of LIGD model, diffusing of the crack zone is limited.

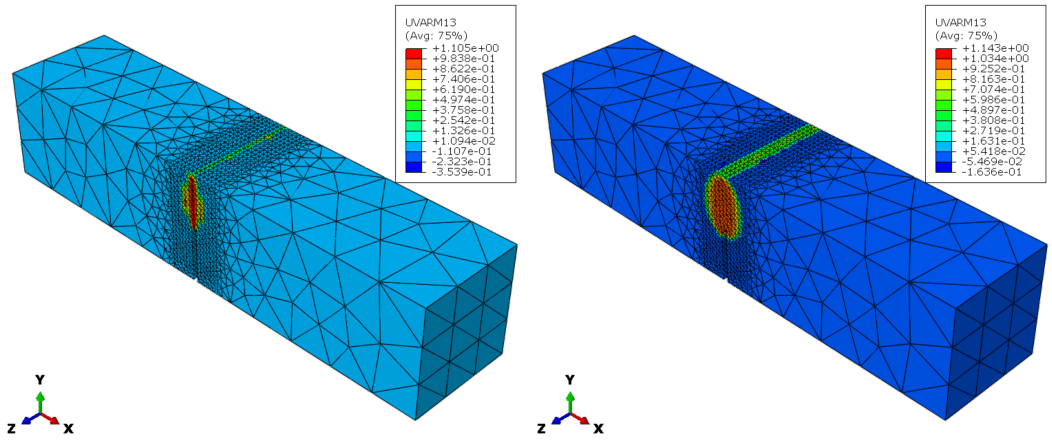

(a) (b)

Figure 4.5. Damage contours of the current study obtained by using (a) LIGD model and (b) CIGD model

4.2. Double Edge Notched Specimen

A double edge notched (DEN) concrete specimen under mixed-mode loading is considered in this example. This experimental setup was proposed and a series of tests were conducted by Nooru-Mohamed, 1992 and a numerical modelling study by using the experimental setup was done by Shedbale et al., 2021 among others. The purpose of using this example is to examine the performance of the two field Bézier tetrahedral element in case of mixed-mode fracture propagation.

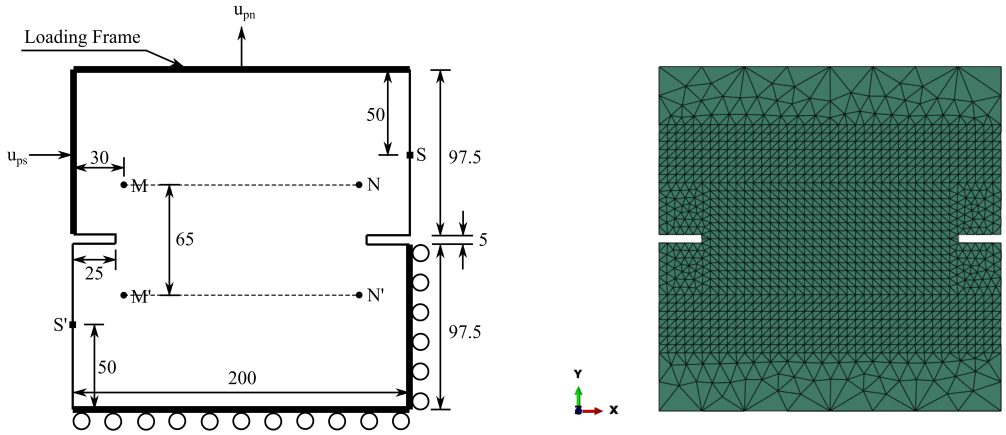

Figure 4.6. Test setup and FE model (a) Test setup with boundary conditions and dimensions (b) FE model used in the analyses

The test setup with its geometrical details and dimensions are presented in Figure 4.6. In the experimental study, there were three types of specimen, but in this study only DEN200 specimen is used. DEN200 has in-plane dimensions of 200 mm x 200 mm and out-of-plane thickness of 50 mm. The specimen has a notch-to-depth ratio of 0.125. The test specimen was fixed to apply tensile and lateral loads by using the loading frame. The boundary conditions are shown in Figure 4.6 as well. By adjusting the vertical and lateral loads, the mixed-mode loading is achieved.

It is to be noted that all of the FEAs conducted in this example are displacement controlled. The prescribed displacements versus time graphs are given in Figure 4.7. The prescribed vertical displacement (u_{pn}) was applied to the top surface of the specimen and prescribed lateral displacement (u_{ps}) was applied to the left surface above the notch,

please see Figure 4.7. These application surfaces are shown in the left hand side in Figure 4.6 as Loading Frame. u_{pn}/u_{ps} ratio is one as proposed in Nooru-Mohamed, 1992. The average relative vertical displacement between MN and M'N' is measured and designated by u_n. Similarly, the lateral displacement between S and S' is taken and denoted by u_s. The finite element model which is used in the analyses is shown in right view (b) in Figure 4.6.

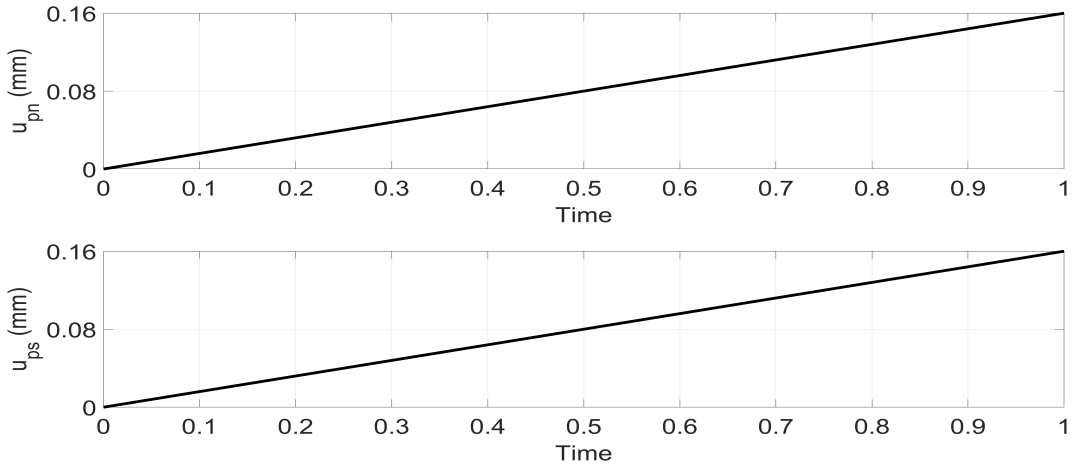

Figure 4.7. Prescribed displacements of u_{pn} and u_{ps} versus time graphs

For this example, both CIGD and LIGD was considered and used in the analyses. Material properties used in this example are given in Table 4.3.

Table 4.3. Used parameters for double edge notched specimen

$E(N/mm^2)$	ν	R	n	β	κ_0	α	l_c	k
30000	0.2	0.005	1	100	9.85E-05	0.96	2	14.4

In order to carry out a mesh convergence study, three analyses with different number of elements were done. The details of the used meshes are given in Table 4.4. After completion of these analyses, the prescribed vertical displacement values (u_{pn}) and the corresponding reaction force values were collected from the top surface of the loading frame in Figure 4.6. The corresponding displacement versus force graphs can be found in Figure 4.8.

The third mesh was selected for further investigations and comparisons with so-

Table 4.4. Used meshes and number of elements for double edge notch specimen

	Total Elements
Mesh #1	24601
Mesh #2	33931
Mesh #3	43904

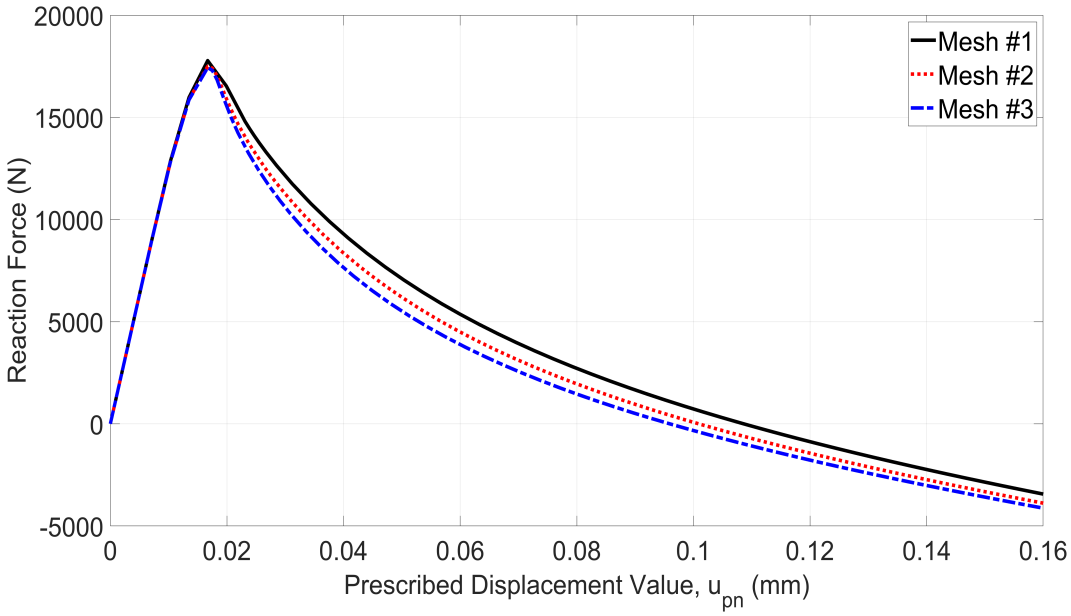

Figure 4.8. Results of mesh convergence study for double edge notch specimen

lutions from different sources. Comparison between the experimental and numerical predictions of other studies and FEA results of current study can be seen in Figure 4.9. By using a similar approach, a comparison for lateral displacement values u_s is shown in Figure 4.10. It is to be noted that, only 2D simulations were done by using 2D quadratic quadrilateral elements with quadratic displacement interpolation and linear interpolation for non-local equivalent strains in Shedbale et al., 2021. However, in the current study, 3D quadratic Bézier tetrahedral elements with a quadratic interpolation for displacements and linear interpolation for non-local equivalent strains both based on Bernstein polynomials are used.

It can be stated that, peak force prediction of the FEA of current study seems sufficient (the values of FEA results of current study and average of experimental results

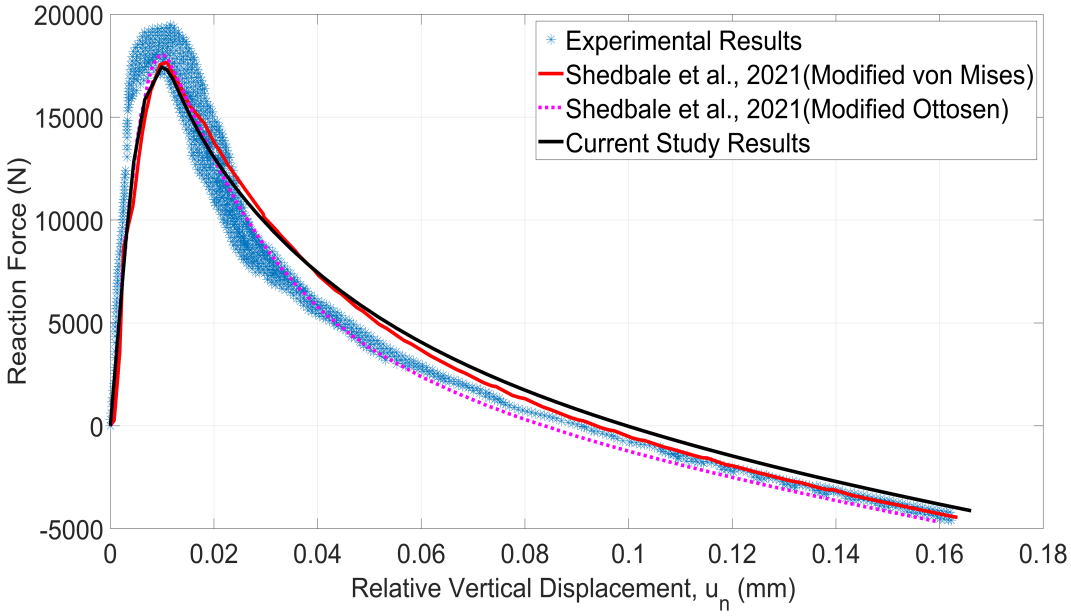

Figure 4.9. Comparison of experimental and numerical results for relative vertical displacement (u_n) versus reaction force values in double edge notch specimen

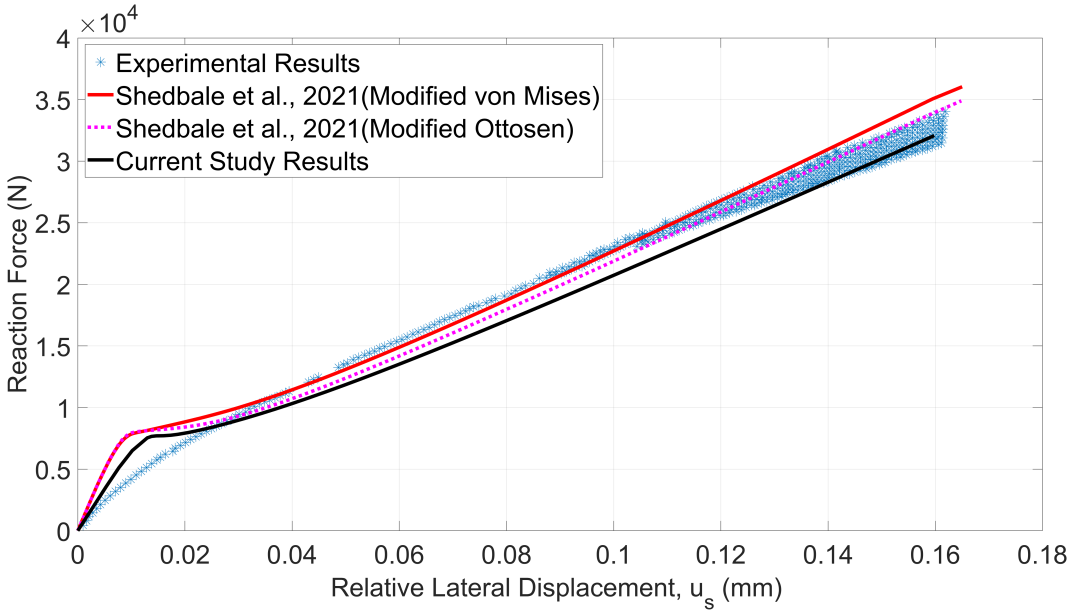

Figure 4.10. Comparison of experimental and numerical results for lateral relative displacement (u_s) versus reaction force values in double edge notch specimen

are 17434N and 18400N, respectively and the difference is around 5.2%). In addition to that, FEA results of current study almost coincide with the numerical results obtained by

using modified von Mises and modified Ottosen non-local equivalent strain definitions in Shedbale et al., 2021. The comparison for vertical displacement u_n versus reaction force and a similar comparison for lateral displacement values u_s versus reaction force graphs are shown in Figures 4.9 and 4.10. Numerical predictions have a clear plateau like region in Figure 4.10, whereas the experimental results do not. The FEA results of the current study give lower reaction values as compared to the results of Shedbale et al., 2021. However, in the last stages of the analysis the predictions of FEA of the current study fall between the results of experimental range.

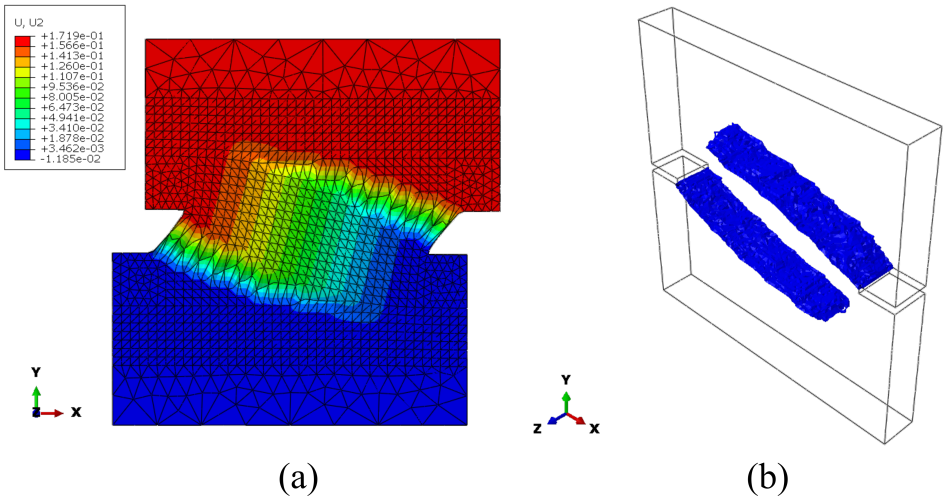

Figure 4.11. Deformed shapes with (a) Vertical Displacement Contour (with a scaling factor of 120) (b) Isometric view of fracture surface

The deformed shape obtained from the FE analysis with vertical displacement contour is located in left hand side of Figure 4.11. The Gauss quadrature point locations with a damage variable of $d \geq 0.90$ and their coordinates were gathered. These coordinate points and the border of the analyzed model were plotted to make a visual representation of the crack surface around the notch. The non-planar behavior of the crack surface is clearly visible in right hand side of Figure 4.11.

In Figure 4.12, the views (a) and (b) the damage contours obtained from LIGD and CIGD are shown next to each other. In view (b) it is clearly seen that the damage zone diffuses to a wide band. It is difficult to identify a sharp crack line. Whereas, in the case of LIGD, widening of the crack zones is suppressed. The agreement between the damage propagation of the FEA of the current study and experimental crack patterns

(black dashed lines) is good. In view (c), the numerical prediction obtained in Shedbale et al., 2021 by using the modified von Mises non-local equivalent strain definition and experimental cracks are shown. The width of the crack zone in view (c) is thinner than LIGD based results of current study. The reason is for this difference is the fact that a much finer FE mesh was used in Shedbale et al., 2021.

In view (c), the numerical prediction obtained in Shedbale et al., 2021 by using the modified von Mises non-local equivalent strain definition and experimental cracks (black dashed lines) taken from Nooru-Mohamed, 1992 are shown. In view (a), the experimental cracks are located on the specimen to compare them with the FEA results of current study.

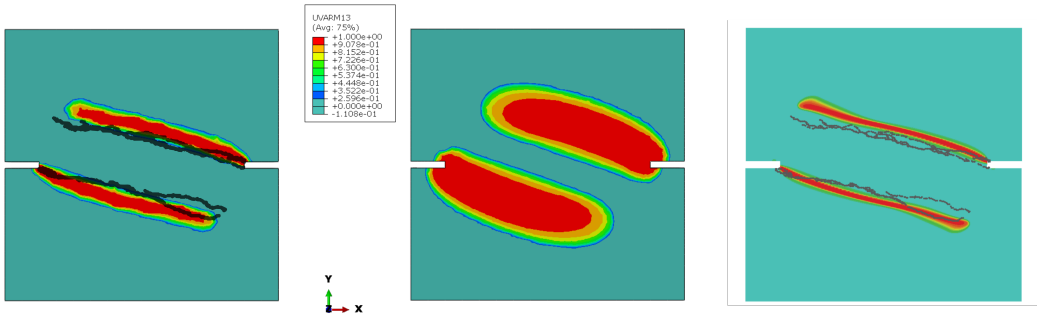

(a) (b) (c)

Figure 4.12. Damage contours of (a) FEA Result of current study with LIGD (b) FEA Result of current study with CIGD (c) Numerical Result of Shedbale et al., 2021. Dotted lines represent experimentally obtained cracks

4.3. Prismatic Concrete Beam Under Eccentric Loading

In this example, a prismatic skew notched concrete beam under eccentric loading is considered. This experimental setup was proposed and a series of tests were conducted by Jefferson et al., 2004 and a numerical study by using the experimental setup was done by Cervera et al., 2017. The purpose of using this example is to examine the sufficiency of the two field Bézier tetrahedral element in case of non-planar crack propagation.

The test setup is shown in Figure 4.13. It is a concrete beam with skew notch clamped with steel frames at both ends. While one of the arms of steel frame is subjected a point loading (at point P in Figure 4.13), the other three arms are restricted in vertical

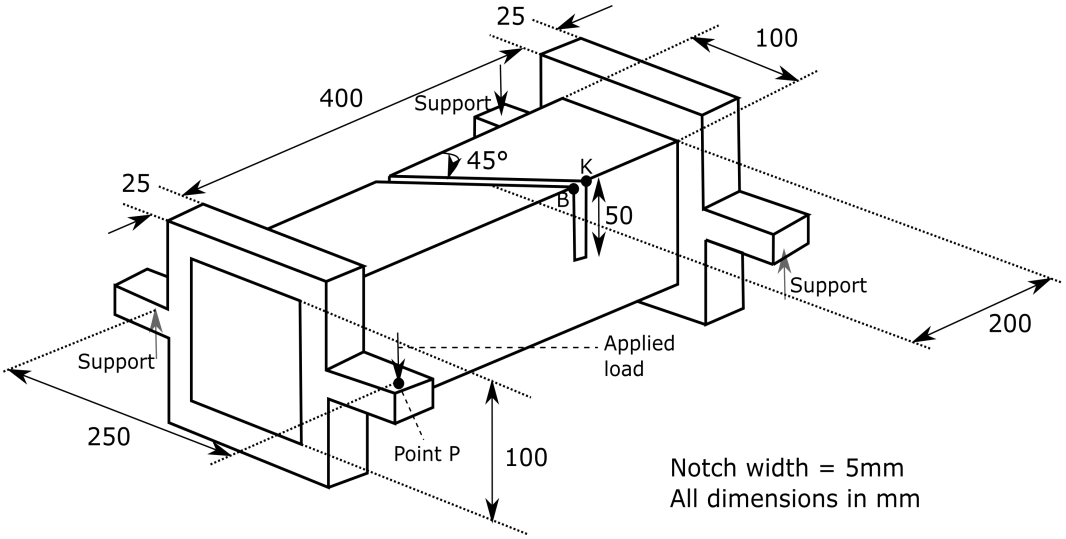

Figure 4.13. Test setup and dimensions for prismatic skew notched concrete beam

direction. Steel frame transfers point load to the concrete beam. The point load creates both torsional and bending moments on the beam.

The finite element model which is used in the analyses with boundary conditions can be seen in Figure 4.14. The steel frames are represented with yellow and concrete beam is represented with green color in the figure. All of the finite element analyses conducted in this example are displacement controlled and prescribed displacement is applied at point P in vertical direction.

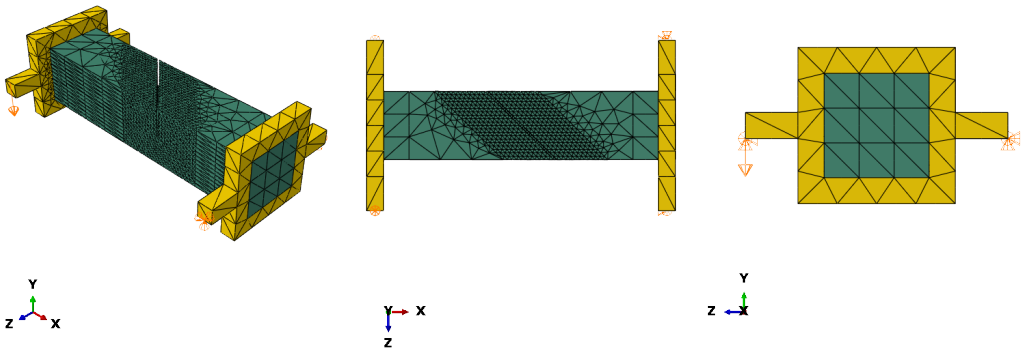

Figure 4.14. Used finite element model in the analysis and its boundary conditions

Steel frames have linear elastic material response and they stay in the elastic re-

gion during the analysis. Modulus of elasticity and Poisson's ratio for steel frames were taken as $E = 200000N/mm^2$ and $\nu = 0.3$, respectively. Material properties used in the concrete beam are represented in the Table 4.5.

Table 4.5. Used parameters for prismatic concrete beam

$E(N/mm^2)$	ν	R	n	β	κ_0	α	l_c	k
35000	0.2	0.005	1	85	9.00E-05	0.96	2	13.9

In order to conduct a mesh convergence study, four analyses with different number of elements were conducted. The details of the used meshes are given in the Table 4.6.

After completion of these analyses, vertical displacement and the reaction force values were collected from the point P. A mesh convergence study is made by using this data and results can be found in Figure 4.15.

The third mesh was selected for further investigations and comparisons with solutions from different sources. For this purposes, the notch mouth opening displacement (also called as crack mouth opening displacement or CMOD) and reaction force at the point P were measured and collected. To measure orthogonal CMOD, distance between the points B and K in Figure 4.13 was stored in every step during the analysis. Comparison between the experiment and finite element analysis for orthogonal CMOD can be seen in Figure 4.16.

Result for the continuum damage model, which is described in a detailed fashion in the previous sections, is shown with black line and experimental results are represented with red stars and blue hexagons in Figure 4.16. It can be stated that, peak force prediction of the FE analysis looks sufficient (the values of FE result and average of experimental

Table 4.6. Used meshes and number of elements for prismatic concrete beam

	Concrete Elements	**Steel Elements**	**Total Elements**
Mesh #1	15966	432	16398
Mesh #2	30095	599	30694
Mesh #3	40184	612	40796
Mesh #4	49483	813	50296

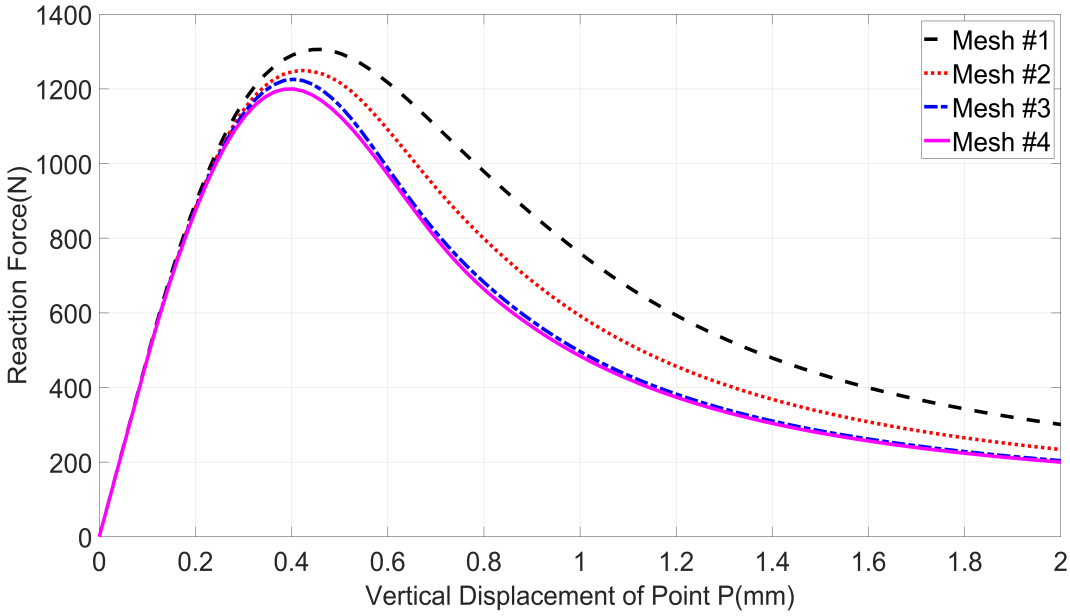

Figure 4.15. Results of mesh convergence study for prismatic skew notched concrete beam

results 1285.2N and 1317.3N, respectively and the difference is around 2.4%). In the post peak regime the FE analysis result falls in between the two experimental curves almost throughout the loading history.

The deformed shape obtained from the FE analysis with vertical displacement contour is located in Figure 4.17.

As mentioned in the beginning of this section, the most challenging part of this example is that the non-planar behavior of the crack surface. Since continuum damage mechanics is used in this thesis, to acquire a significant failure surface is not possible. However, a crack surface can be represented by using the damage variables in integration points. For this purpose, the Gauss quadrature point locations with a damage variable of $d \geq 0.99$ and their coordinates were gathered. These coordinate points and the border of the analyzed model were plotted to make a visual representation of the crack surface around the notch. In Figure 4.18, side view of fracture surfaces obtained from current FEA and reference solution are represented.

The results from the experiment which was conducted in the previously mentioned paper and FEA with both conventional and localizing implicit gradient damage model is shown in Figure 4.19. The non-planar crack surface is visible both in the localizing

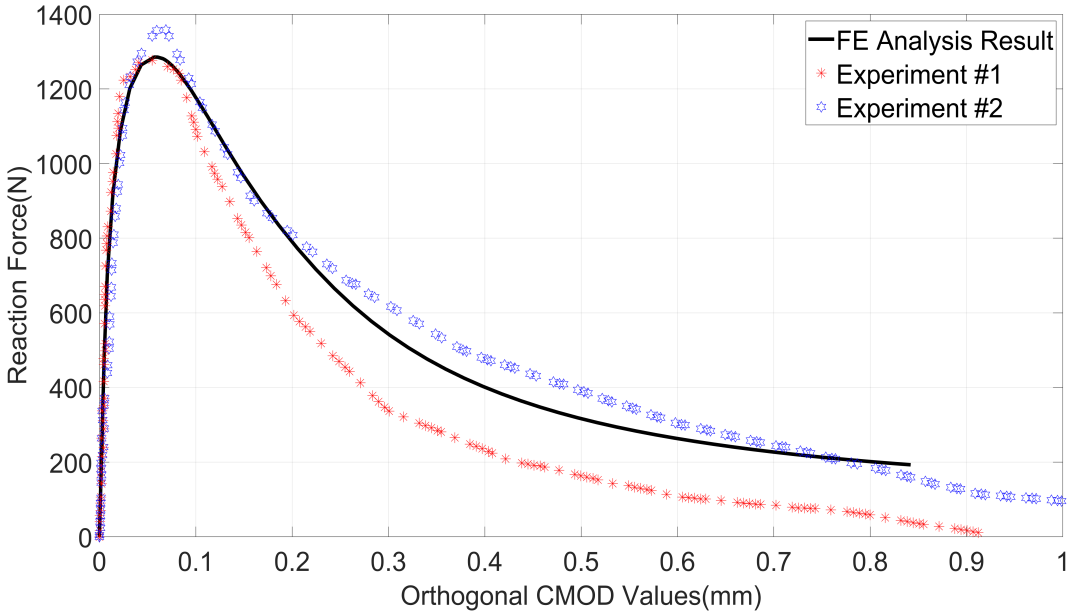

Figure 4.16. Comparison of analysis and experiment results for orthogonal CMOD for prismatic skew notched concrete beam

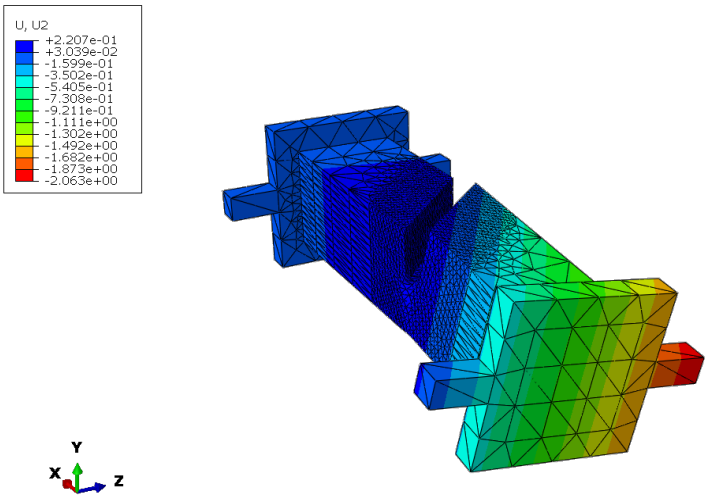

Figure 4.17. The deformed shape of analysis with vertical displacement contour plot

implicit gradient damage model and experimental results. However, crack surface cannot be predicted properly by using the conventional implicit gradient damage model. The used two field Bézier tetrahedral element mentioned in Section 3.2 and localizing implicit gradient damage model defined in Section 2.6 seem to be successful to predict even for

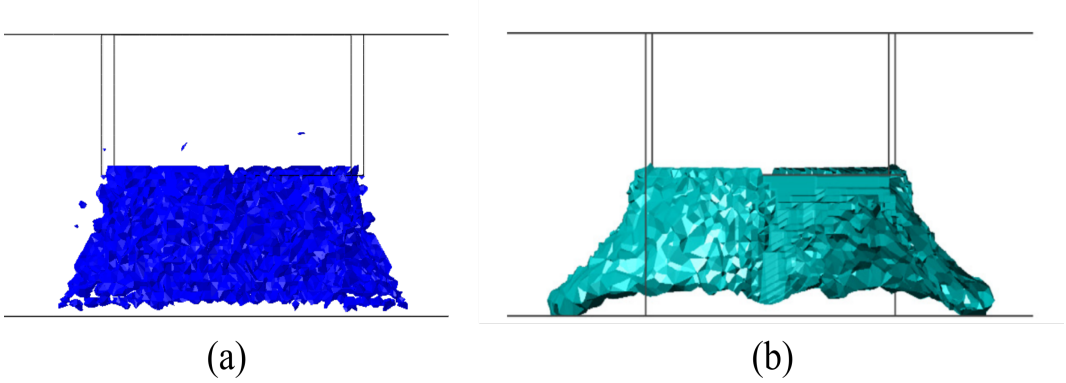

Figure 4.18. Side view of the fracture surfaces (a) FE Analysis result for defined model in this study (b) FE Analysis result of reference paper

challenging non-planar crack cases.

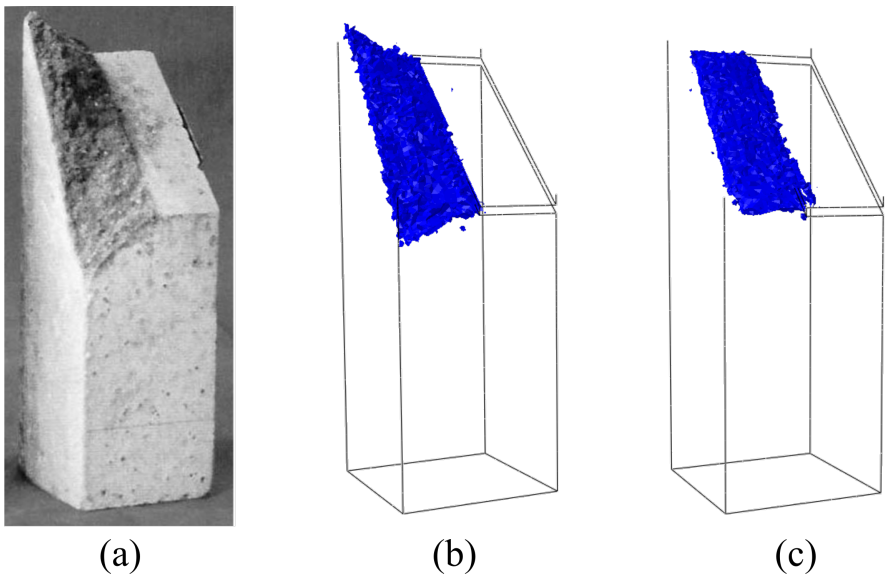

Figure 4.19. Experimental and finite element analysis results. The non-planar behavior of crack surface in localizing model coincides with the experimental result. However, non-planar behavior cannot be seen in conventional model. (a) Experimental Result (b) Localizing Model (c) Conventional Model

As can be seen in Figure 4.20, the comparison between the conventional and localizing implicit gradient damage model results are presented. To compare the predictions of these two models please see the Figure 4.20. The crack surface obtained by using the con-

ventional model is wide and non-planar behavior is not obvious. Whereas the localizing model yields a thin and non-planar crack surface.

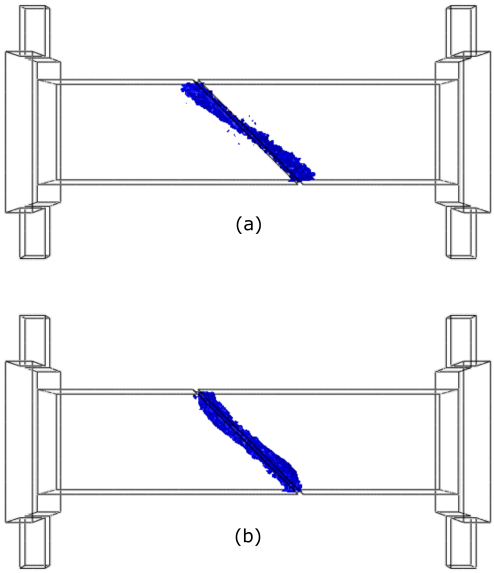

Figure 4.20. Comparison of crack surfaces obtained from conventional and localizing implicit gradient damage models (a) Localizing (b) Conventional

4.4. Cylindrical Concrete Beam Under Eccentric Loading

In this example, a cylindrical skew notched concrete beam under eccentric loading is considered. This experimental setup was proposed and a series of tests were conducted by Jefferson et al., 2004 and a numerical study by using the experimental setup was done by Cervera et al., 2017 similar to the example considered in Section 4.3. The purpose of using this example is same as the previous one and is to examine the accuracy of the two field Bézier tetrahedral element in case of non-planar crack propagation.

The test setup is shown in Figure 4.21. It is a cylindrical concrete beam with skew notch clamped from both ends by using steel frames. One of the arms of steel frame is subjected a point loading (at point P in Figure 4.21), the other three arms are fixed in vertical direction. The point load creates both torsional and bending moments on the beam.

The finite element model which is used in the analyses with boundary conditions

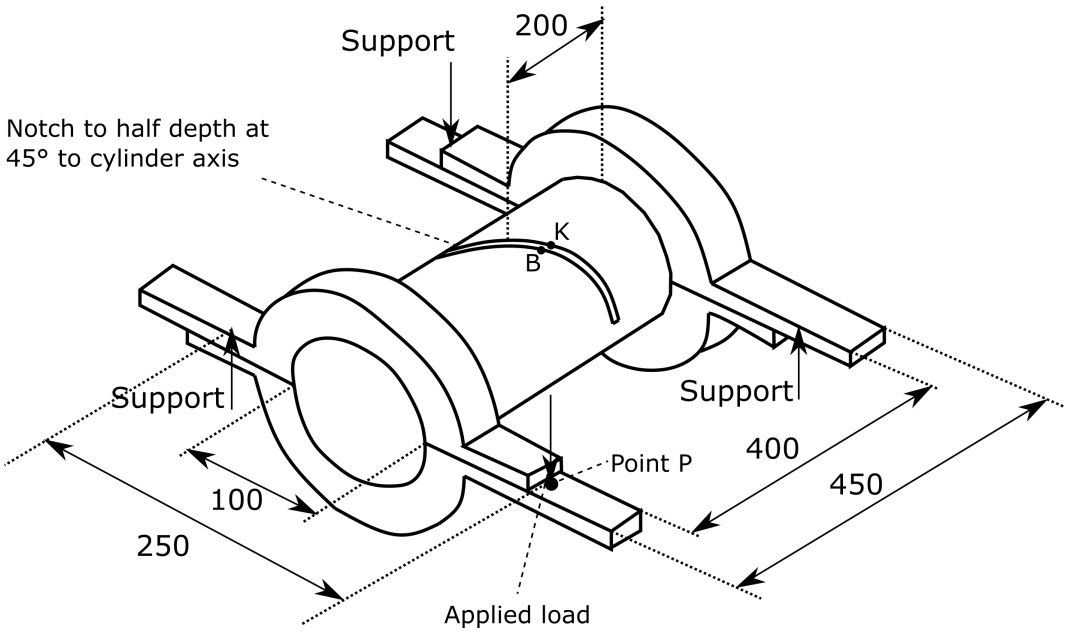

Figure 4.21. Test setup and dimensions for cylindrical skew notched concrete beam

Table 4.7. Used meshes and number of elements for cylindrical concrete beam

	Concerete Elements	**Steel Elements**	**Total Elements**
Mesh #1	20996	587	21583
Mesh #2	30077	574	30651
Mesh #3	43143	582	43725
Mesh #4	57441	582	58023

are shown in Figure 4.22. The steel frames are demonstrated with yellow and concrete beam with green color in the figure. All of the finite element analyses conducted in this example are displacement controlled and prescribed displacement is applied at point P in vertical direction.

It is important to note that, this specimen and previous rectangular skew notched beam specimen were tested in same experimental study for both specimens same materials were used. Therefore material properties for steel and concrete materials are same as the ones given in Section 4.3 and Table 4.5.

In order to carry out a mesh convergence study, four analyses with different number of elements were done. The details of the used meshes are given in the Table 4.7.

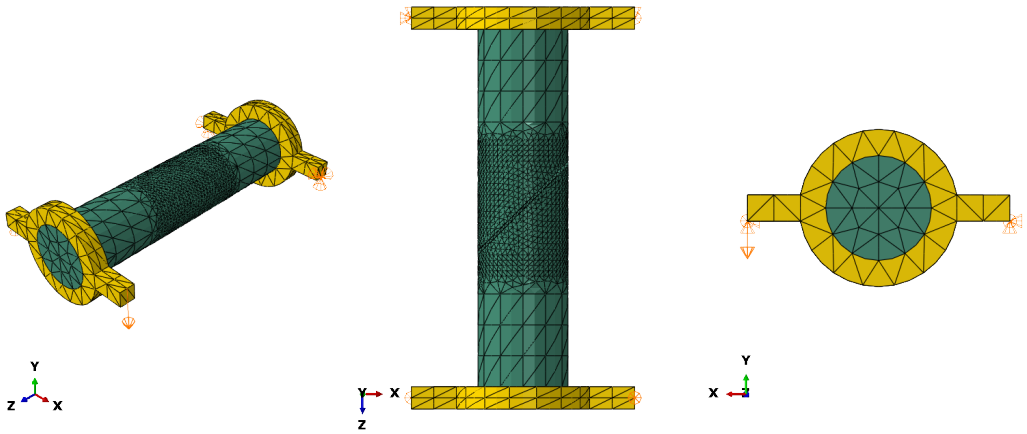

Figure 4.22. Used finite element model in the analysis from different point of views and its boundary conditions

In Figure 4.23, vertical displacement versus reaction force values obtained from Point P for different meshes are presented. From these reaction force versus displacement curves it is clearly seen that response converges a certain curve upon mesh refinement.

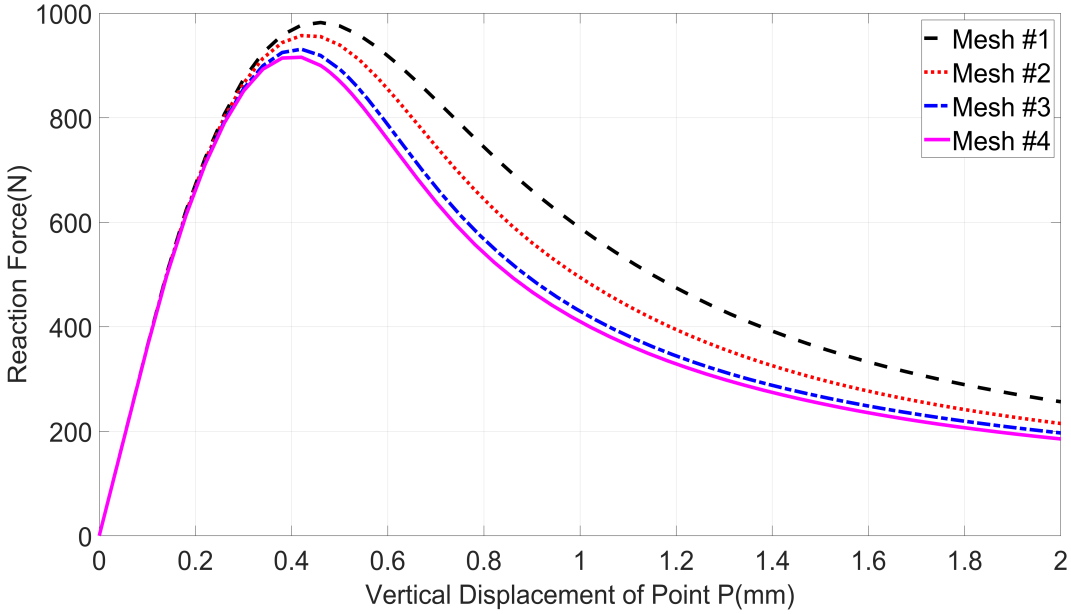

Figure 4.23. Results of mesh convergence study for cylindrical skew notched concrete beam

The third mesh was chosen for further investigations and comparisons with solutions from different sources mentioned in the previous section. Following the similar

step explained in Section 4.3, CMOD is calculated and the resulting CMOD versus reaction force graph is represented in Figure 4.24 along with the experimental and numerical results.

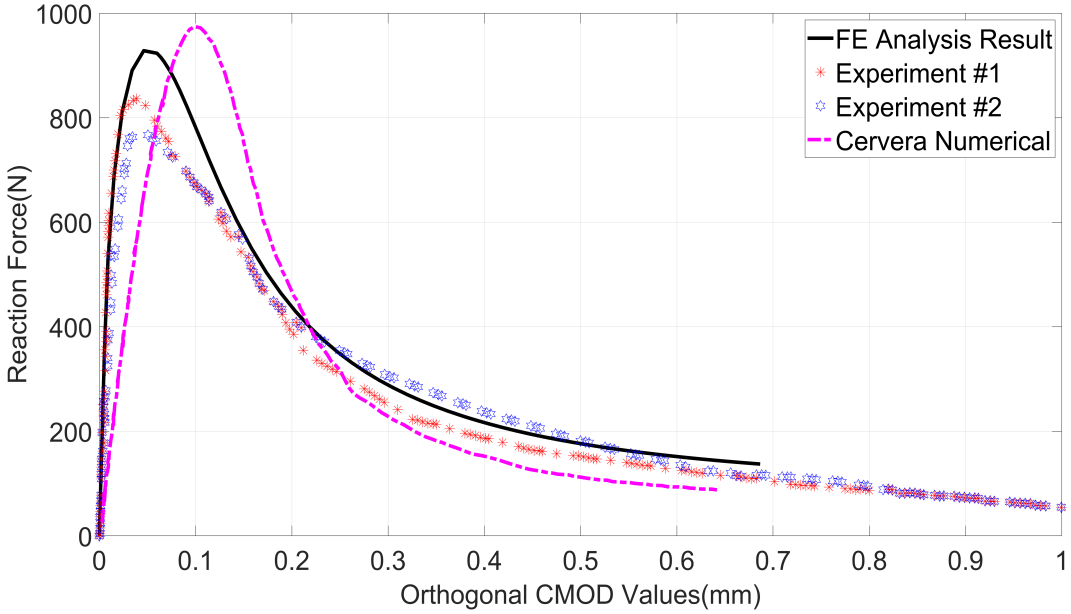

Figure 4.24. Comparison of analysis and experiment results for orthogonal CMOD for cylindrical skew notched concrete beam

It can be stated that, peak force prediction of the FE analysis looks higher than the experimental results (the values of FE result and average of experimental results 928.3N and 801.5N, respectively and the difference is almost 13.6%). In the post peak regime the FE analysis result falls in between the two experimental curves almost throughout the loading history.

Similar to the previous example, crack surface is generated by collecting the damage variables in integration points. For this representation, the Gauss quadrature point locations with a damage variable of $d \geq 0.99$ and their coordinates were brought together. These coordinate points and the border of the model were displayed to obtain a visual representation of the failure surface around the notch. In Figure 4.25, different views of the fracture surface obtained from FEA and reference solution are presented.

In Figure 4.25, crack surface obtained by using the CIGD is also shown. From the comparison of experiment, CIGD and LIGD crack surface, it can be clearly stated that LIGD is performing better than CIGD in predicting the crack surface. The crack surface

constructed from the CIGD is thicker and non-planar crack surface is not obvious. On the other hand LIGD yields a thinner and non-planar failure crack surface.

It is also to be noticed that the previous and the current examples have a strong dependency on the applied boundary conditions. Changes on applied boundary conditions affect the obtained results dramatically.

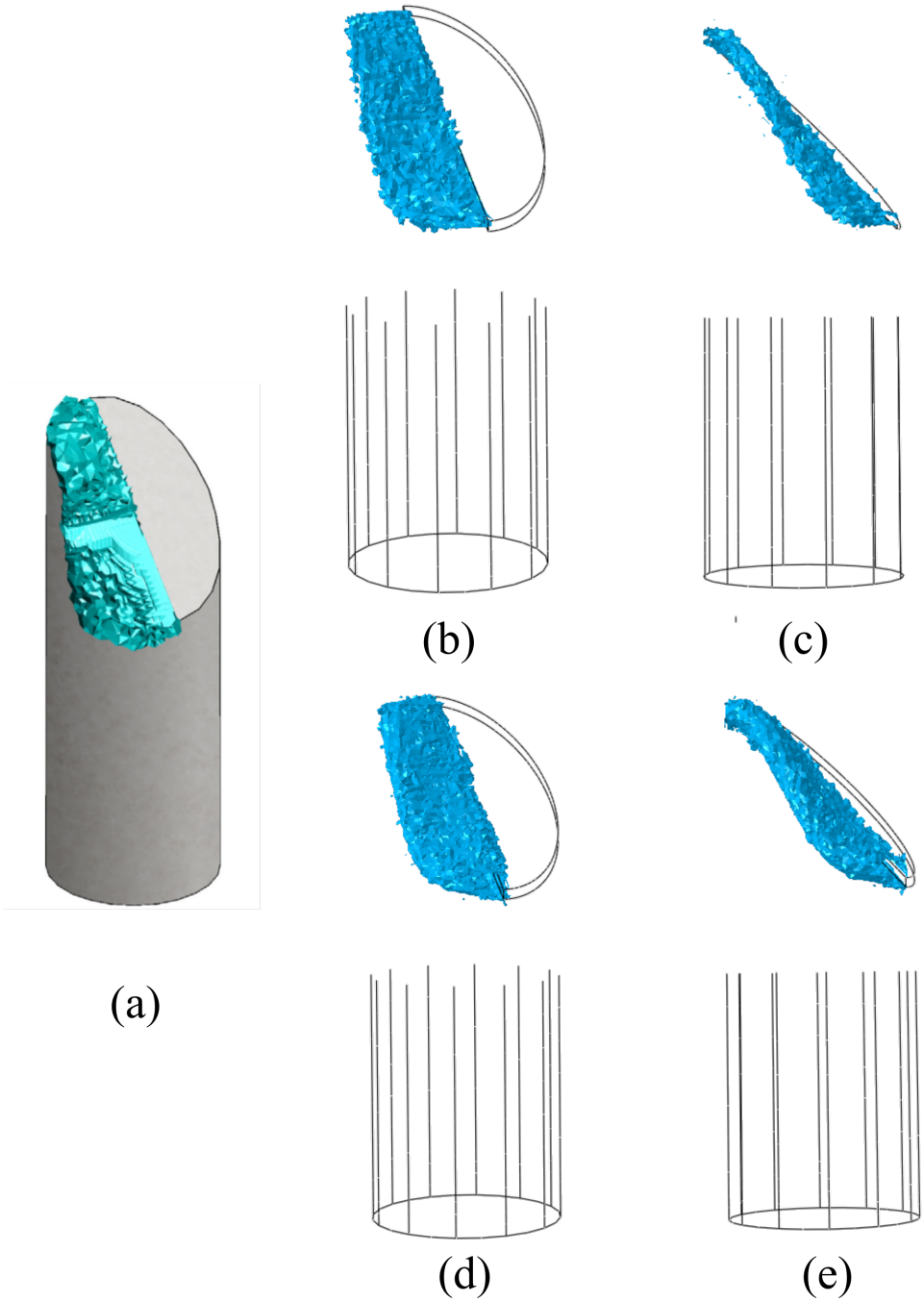

Figure 4.25. Experimental and finite element analysis results. The non-planar behavior of crack surface in localizing model fits with the experimental result. But, non-planar behavior cannot be predicted by using conventional model. (a) Experimental Result (b) Localizing Model from front side (c) Localizing Model from another side (d) Conventional Model from front side (e) Conventional Model from another side

CHAPTER 5

CONCLUSION AND OUTLOOK

5.1. Summary and Main Findings

In this thesis, main task was the implementation of two field formulation with a tetrahedral geometry for damage mechanics based failure analysis of quasi-brittle structural components. To this end, LIGD formulation was embedded within a quadratic Bézier tetrahedral element and implemented to Abaqus through user defined element subroutine. Before failure analysis of quasi-brittle structural components, two benchmark problems were analyzed to validate the performance of the implemented element and compared with the library element of Abaqus. Afterwards, the performance of implemented element was investigated by means of 3D case studies. The main findings of the study can be listed as follows;

- Implemented quadratic 3D Bézier tetrahedral element performed as good as quadratic hexahedral element of Abaqus. The performance of the conventional quadratic tetrahedral and quadratic Bézier tetrahedral element are close. Since Kadapa, 2019a compared quadratic Bézier tetrahedral elements with conventional linear tetrahedral ones, the performance of quadratic Bézier tetrahedral element seems to be very good as compared to conventional tetrahedral element. However this comparison given in Kadapa, 2019a is not appropriate since quadratic and linear elements are compared.

- The results obtained from benchmark problems almost coincided with the reference solution for both elastic and elasto-plastic material responses.

- 10 noded quadratic 3D Bézier tetrahedral element and LIGD model combination gave sufficient results in case of both planar and nonplanar fracture propagation. The results obtained from the first example with LIGD model were very close to experimental results. The difference of peak responses was calculated around 2.8%

and the post peak response of current study stayed slightly higher than the experimental results. A thin and planar crack surface is obtained. In the second example, the difference of peak responses was around 5.2% and post peak response was close to the experimental study for both vertical and horizontal responses. Furthermore, the resulting crack surface is non-planar and the propagation of the fracture can be considered precise as compared to the experimental observations. In the third example, the difference of peak responses was calculated around 2.4%. In the post peak regime the analysis result falls in between the two experimental curves almost during the whole loading history. With the aid of the LIGD model, a thin and non-planar fracture surface was obtained with very similar orientation to the experimental one. The difference of peak responses was computed around 13.6% for the last example. The result obtained in the post peak regime remains between the experimental responses. A non-planar failure surface was obtained by using LIGD model, however it was not possible to reach a thin crack surface by using CIGD model. In all of the cases, with the LIGD model the crack paths are confined to a relatively thin layers, whereas in case of CIGD, diffusion of damage is clearly visible.

5.2. Recommendations for Future Studies

In this thesis, a study has been carried out on a subject that is still open to development. The recommendations for future studies can be summarized as follows;

- Bernstein polynomials are non-negative in the whole range they are defined. With the aid of this property, their usage as basis polynomials can prevent the existence of negative components in mass matrices. Therefore, the presented Bézier tetrahedral element can be extended to dynamics for both explicit and implicit analysis.
- As mentioned previously, the analysis results have a strong dependency on application of boundary conditions. Comparison of the effects of applied boundary conditions can be considered as a future study.
- The evolution equation for damage variable is not physically well motivated. There

are fitting parameters both for CIGD and LIGD formulations which are not related to experimentally measured fracture parameters directly (e.g., fracture energy). Therefore, damage models where fracture energy and strength parameters are directly used would be much more useful.

- This study can be extended to analyze the reinforced concrete structural components. For this purpose, rebars can be modeled explicitly as 3D solid body or can be embedded in the bulk as rebar elements.

- In this study, the modified von Mises equivalent strain was used. However, there are also different equivalent strain definitions in the literature. The predictions of different equivalent strain measures can be investigated as well.

REFERENCES

Bathe, K.-J. (Ed.) (2014). *Finite element procedures* (2nd edition ed.). Watertown, MA: K.J. Bathe.

Bažant, Z. P., T. B. Belytschko, and T.-P. Chang (1984, December). Continuum Theory for Strain-Softening. *Journal of Engineering Mechanics 110*(12), 1666–1692.

Beer, G. (2015). *Isogeometric Methods for Numerical Simulation*. Number vol. 561 in CISM courses and lectures. Wien: Springer.

Benedetti, L., M. Cervera, and M. Chiumenti (2017, May). 3D numerical modelling of twisting cracks under bending and torsion of skew notched beams. *Engineering Fracture Mechanics 176*, 235–256.

Brekelmans, W. A. M., P. J. G. Schreurs, and J. H. P. de Vree (1992, March). Continuum damage mechanics for softening of brittle materials. *Acta Mechanica 93*(1-4), 133–143.

Cervera, M., G. B. Barbat, and M. Chiumenti (2017, November). Finite element modeling of quasi-brittle cracks in 2D and 3D with enhanced strain accuracy. *Computational Mechanics 60*(5), 767–796.

Cervera, M., M. Chiumenti, and R. Codina (2011, September). Mesh objective modeling of cracks using continuous linear strain and displacement interpolations: Mesh Objective Modeling of Cracks. *International Journal for Numerical Methods in Engineering 87*(10), 962–987.

Cottrell, J. A., T. J. R. Hughes, and Y. Bazilevs (2009). *Isogeometric analysis: toward integration of CAD and FEA*. Chichester, West Sussex, U.K. ; Hoboken, NJ: Wiley. OCLC: ocn335682757.

Cox, M. G. (1972). The Numerical Evaluation of B -Splines. *IMA Journal of Applied*

Mathematics 10(2), 134–149.

de Boor, C. (1972, July). On calculating with B-splines. *Journal of Approximation Theory 6*(1), 50–62.

de Vree, J., W. Brekelmans, and M. van Gils (1995, May). Comparison of nonlocal approaches in continuum damage mechanics. *Computers & Structures 55*(4), 581–588.

Engvall, L. and J. A. Evans (2016, June). Isogeometric triangular Bernstein–Bézier discretizations: Automatic mesh generation and geometrically exact finite element analysis. *Computer Methods in Applied Mechanics and Engineering 304*, 378–407.

Engvall, L. and J. A. Evans (2017, June). Isogeometric unstructured tetrahedral and mixed-element Bernstein–Bézier discretizations. *Computer Methods in Applied Mechanics and Engineering 319*, 83–123.

Espath, L. F. R., A. L. Braun, and A. M. Awruch (2011). An Introduction to Isogeometric Analysis Applied to Solid Mechanics. pp. 21.

Farin, G. E. and G. E. Farin (1999). *NURBS: from projective geometry to practical use* (2nd ed ed.). Natick, Mass: A.K. Peters.

Hughes, T. J. R. (1987). *The finite element method: linear static and dynamic finite element analysis*. Englewood Cliffs, N.J: Prentice-Hall.

Jefferson, A., B. Barr, T. Bennett, and S. Hee (2004, August). Three dimensional finite element simulations of fracture tests using the Craft concrete model. *Computers and Concrete 1*(3), 261–284.

Jirásek, M. (1998, November). Nonlocal models for damage and fracture: Comparison of approaches. *International Journal of Solids and Structures 35*(31-32), 4133–4145.

Kadapa, C. (2019a, February). Novel quadratic Bézier triangular and tetrahedral elements using existing mesh generators: Applications to linear nearly incompressible elastostatics and implicit and explicit elastodynamics: Novel Bézier elements for nearly incompressible linear elasticity. *International Journal for Numerical Methods in Engineering 117*(5), 543–573.

Kadapa, C. (2019b, July). Novel quadratic Bézier triangular and tetrahedral elements using existing mesh generators: Extension to nearly incompressible implicit and explicit elastodynamics in finite strains. *International Journal for Numerical Methods in Engineering 119*(2), 75–104.

Khoei, A. R. (2015). *Extended finite element method: theory and applications*. Chichester, West Sussex: John Wiley & Sons, Inc.

Mazars, J. and G. Pijaudier-Cabot (1989, February). Continuum Damage Theory—Application to Concrete. *Journal of Engineering Mechanics 115*(2), 345–365.

Mediavilla Varas, J. (2005). Continuous and discontinuous modelling of ductile fracture. Publisher: Technische Universiteit Eindhoven.

Nguyen, V. P., C. Anitescu, S. P. Bordas, and T. Rabczuk (2015, November). Isogeometric analysis: An overview and computer implementation aspects. *Mathematics and Computers in Simulation 117*, 89–116.

Nguyen, V. P. and H. Nguyen-Xuan (2013, August). High-order B-splines based finite elements for delamination analysis of laminated composites. *Composite Structures 102*, 261–275.

Nooru-Mohamed, M. B. (1992). *Mixed-mode fracture of concrete: an experimental approach*.

Peerlings, R. H. J. (2008). Continuum damage mechanics lecture notes. Publisher: Department of Mechanical Engineering, Eindhoven University of Technology, Eind-

hoven, The Netherlands.

Peerlings, R. H. J., R. de Borst, W. A. M. Brekelmans, and M. G. D. Geers (1998, October). Gradient-enhanced damage modelling of concrete fracture. *Mechanics of Cohesive-frictional Materials 3*(4), 323–342.

Perduta, A. and R. Putanowicz (2019, January). Tools and techniques for building models for isogeometric analysis. *Advances in Engineering Software 127*, 70–81.

Piegl, L. A. and W. Tiller (1997). *The NURBS book* (2nd ed ed.). Monographs in visual communications. Berlin ; New York: Springer.

Pietruszczak, S. and Z. Mróz (1981, March). Finite element analysis of deformation of strain-softening materials. *International Journal for Numerical Methods in Engineering 17*(3), 327–334.

Poh, L. H. and G. Sun (2017, May). Localizing gradient damage model with decreasing interactions: Localizing Gradient Damage Model with Decreasing Interactions. *International Journal for Numerical Methods in Engineering 110*(6), 503–522.

Sarkar, S., I. Singh, B. Mishra, A. Shedbale, and L. Poh (2019, August). A comparative study and ABAQUS implementation of conventional and localizing gradient enhanced damage models. *Finite Elements in Analysis and Design 160*, 1–31.

Shedbale, A. S., G. Sun, and L. H. Poh (2021, June). A localizing gradient enhanced isotropic damage model with Ottosen equivalent strain for the mixed-mode fracture of concrete. *International Journal of Mechanical Sciences 199*, 106410.

Zienkiewicz, O. C., R. L. Taylor, and D. Fox (2014). *The finite element method for solid and structural mechanics* (7th ed ed.). Amsterdam ; Boston: Elsevier/Butterworth-Heinemann. OCLC: ocn858011693.

Zienkiewicz, O. C., R. L. Taylor, and J. Z. Zhu (2013). *The finite element method: its basis and fundamentals* (Seventh edition ed.). Amsterdam: Elsevier, Butterworth-

Heinemann. OCLC: ocn852808496.